Curvilinear 2|3D finite elements for the analysis of shells with arbitrary curvature and variable thickness

Computers and Structures 317 (2025) 107911

Contents lists available at ScienceDirect

Computers and Structures

journal homepage: www.elsevier.com/locate/cas

Curvilinear 2|3D finite elements for the analysis of shells with arbitrary curvature and variable thickness

Piero Chiaia [a,*], Maria Cinefra [b], Erasmo Carrera [a]

[a] MUL² Lab, Department of Mechanical and Aerospace Engineering, Politecnico di Torino, Corso Duca degli Abruzzi 24, 10129, Torino, Italy
[b] Department of Mechanics, Mathematics and Management, Politecnico di Bari, Via Edoardo Orabona, 4, 70126, Bari, Italy

ARTICLE INFO

Keywords:
Finite element method
Carrera unified formulation
Curvilinear models
Shell models
Variable thickness
Variable curvature

ABSTRACT

This paper presents a novel curvilinear finite element (FE) formulation for the static and modal analysis of shells with arbitrary curvature and variable thickness. In the proposed approach, high-order 2D shell models are defined in three curvilinear coordinates, exploiting the co- and contravariant components of physical quantities in the non-orthogonal reference frame. The Carrera Unified Formulation (CUF) is adopted for the definition of 2D shell models in which Lagrange functions are employed for the through-the-thickness approximation of displacements; then, merging CUF with finite element approximation of midsurface, new 3D-like FE elements are generated in which different orders of expansion can be adopted along the three curvilinear coordinates. For this reason, these elements are referred to as 2|3-D because they present both the computational efficiency of 2D models and the capability to model non-orthogonal geometries, such as shells with variable thickness, of 3D elements. Geometrical relations are derived within the classical differential geometry framework, and weak-form equilibrium equations are derived through the Principle of Virtual Displacements (PVD). The capabilities of the present finite elements are investigated by performing the static and modal analysis of various shell-like structures. The accuracy of the present approach in terms of three-dimensional stress states and natural frequencies is demonstrated by comparing the numerical results with solutions obtained by classical 3D finite elements using commercial software, highlighting the computational efficiency of the present elements. Finally, the proposed methodology is applied to analyze complex engineering applications.

1. Introduction

In modern engineering applications, the Finite Element Method (FEM) is a widely adopted numerical method for solving complex engineering problems involving structural mechanics, heat transfer, and multi-physics interactions [1]. Due to its versatility, this method is extensively used in many engineering fields to predict the structural response of different materials and structures under various loading conditions, and it has been widely adopted for exploring novel design features in the context of optimization problems [2–4]. In more recent applications, the FEM has also been adopted to investigate novel geometrical configurations featuring geometrical variations, see [5,6]. Numerical simulations are therefore widely used to analyze innovative configurations' mechanical behavior and the design of high-performance structures [7,8].

In aerospace engineering, variable thickness structures are extensively used in the design of aircraft wings, fuselages, and spacecraft components to maintain structural integrity and optimize weight. Similarly, in mechanical engineering, components such as rotating disks and rotors [9], and automotive panels benefit significantly from variable geometrical features. In biomedical engineering, prosthetics, implants, and orthopedic devices rely on variable geometrical features to mimic the natural biomechanical behavior of tissues and bones [10]. The design approach allowed by such geometrical features permits improving structural and thermal performance, contributes to cost-effective material usage, and allows better compliance with complex design and loading conditions.

In the context of numerical simulations, already available one- and two-dimensional beam and plate/shell formulations are established under classical kinematic assumptions, such as the Euler-Bernoulli beam theory (EBBT) or classical plate theories like the first-order shear deformation theory (FSDT) [11]. However, classical structural theories are unsuitable for shear deformable structures, and typically higher-order

* Corresponding author.
Email addresses: piero.chiaia@polito.it (P. Chiaia), maria.cinefra@poliba.it (M. Cinefra), erasmo.carrera@polito.it (E. Carrera).

https://doi.org/10.1016/j.compstruc.2025.107911
Received 14 April 2025; Accepted 28 July 2025
Available online 6 August 2025

theories are required [12,13]. Although these models provide reasonable accuracy and theoretically consistent results, the imposed kinematic assumptions are unsuitable when complex structures exhibiting thickness variations, curvature, or material anisotropy are analyzed [14,15]. As a result, the standard finite elements are not suitable for the analysis of such structures and suffer from numerical issues such as shear locking, membrane locking, Poisson locking, and trapezoidal locking [16–18]. In the field of high-fidelity numerical simulation of complex structures, curvilinear finite element formulations have been proposed over the years to incorporate a geometry-adaptive approach, both for beam [19–21] and plate/shell [22–25] structural elements.

Many approaches have also been proposed in the literature to analyze curved shells with variable thickness [26–28]. Within this context, the influence of geometry variation alongside the effect of curvature on the global mechanical response of the structure becomes a novel computational challenge due to the aforementioned numerical problems arising in such finite element formulations [29]. As stated by Simo et al. [30], the incorporation of thickness stretch inside the finite element models is given by the simplicity of implementing a fully three-dimensional constitutive model. In this context, the effects of arbitrary thickness variation on the structural response have been investigated by many authors, see [31–33].

Generally, the analysis of complex structures in the framework of non-constant geometrical features can be handled by adopting classical 3D finite element formulations since, nowadays, CAD (Computer-Aided Design) systems are integrated with the FE framework. However, adopting such models leads to computationally burdensome models and the adoption of refined meshes [34], especially in the case of thin-walled structures or ultra-thin laminates due to well-known aspect ratio constraints and lower-order polynomial order of interpolations.

In recent years, shell models have also been implemented in the well-established Carrera Unified Formulation [35]. Within this framework, 2D shell models have been implemented in a recursive index formalism that allows the straightforward implementation of any possible theory of structure approximation. Equivalent-Single-Layer (ESL) and Layer-Wise (LW) theories have already been implemented within the CUF-based 2D shell theory [36], investigating the influence of lower to higher orders of expansion along the thickness direction. The capabilities of the present approach have been assessed in many works, see [37,38]. In the Unified formulation of shell theories, FE models are defined hierarchically and regardless of the structural theory employed. Starting from the Principle of Virtual Displacement (PVD), the governing equations are written in terms of invariants of the kinematic model and structural theory adopted, the Fundamental Nuclei (FN) [35]. In addition, the CUF formalism has introduced the Node-Dependent Kinematic (NDK) approach. Under the NDK approach, allowed by CUF, the thickness expansion functions can be directly assigned at the nodal level of the 2D shell finite element adopted in the mid-surface discretization, assigning then to each FE node its theory of structure approximation of any order [39]. Therefore, local refinements can be straightforwardly implemented by assigning higher-order theories of structures where needed in a resulting pure displacement-based FE model. Thanks to the hierarchical nature of the FN, the governing equations in matrix form are directly obtained by exploiting the recursive index notation [40], without any need for coupling techniques. The different expansion fields adopted in different finite nodes are then coupled with the classical FE shape functions, ensuring continuity and smooth transition between the different displacement fields, defined locally.

The present work proposes extending CUF shell models in a general curvilinear reference frame to analyze variable thickness shells with arbitrary curvature. In the proposed FE formulation, the isoparametric approach is adopted, namely using the same polynomial expansion for the geometric interpolation and displacement interpolation [41]. Thus, a local computation of the covariant and contravariant physical quantities is achieved under a hierarchical expression that uses the CUF approximation in a 3D sense, exploiting the possibility of adopting different polynomial expansion orders in different directions. Exploiting the NDK approach, any variation in structural geometrical features can be naturally embedded in the element without ad-hoc techniques. The physical quantities required for the computation of FE matrices are computed in the non-orthogonal curvilinear reference frame, reconstructing the classical Cartesian coordinate features through a transformation law. The final governing equations for the linear static and modal analysis are written in terms of FN, matrices independent of the structural theory adopted, and the kinematic assumption of the element.

The work is organized as follows: (i) the mathematical preliminaries and the introduction to the differential geometry approach used are presented in Section 2; (ii) classical shell models within the CUF approach and the extension of the NDK approach to shell structures are described in Section 3; (iii) the proposed isoparametric approach for the 3D description of the geometry and the displacement field is presented in Section 4; (iv) the governing equations for the pure mechanical analysis of linear elastic structures are derived through the Principle of Virtual Displacements (PVD) and rewritten in terms of FN, as described in Section 5; (v) three different numerical examples dealing with variable thickness and variable curvature shells are presented and analyzed in Section 6; (vi) the conclusions are finally discussed in Section 7.

2. Mathematical preliminaries

This section presents the general mathematical framework adopted to define the present FE formulation. Here, the geometrical quantities involved in defining the numerical method are introduced, focusing on the covariant and contravariant components of vectors and the general differential operators. Stress and strain components are derived in the non-orthogonal curvilinear general framework and then recovered in Cartesian components.

2.1. Curvilinear coordinates

Let $\mathbf{\Omega}_0$ be the reference configuration of a continuum body, namely the undeformed state. Denote also with $\mathbf{\Omega}$ the actual deformed configuration of the body after the deformation process. Let $\mathbf{P}^{(0)}$ be a material point in the reference configuration, described by the position vector $\boldsymbol{X}$ with respect to the global Cartesian reference frame with basis vectors $(\mathbf{i}_1, \mathbf{i}_2, \mathbf{i}_3)$. Denote also with $\mathbf{P}$ the associated point in the deformed actual configuration described by the position vector $\boldsymbol{x}$. The arbitrary position vector can be rewritten in terms of local curvilinear coordinates by defining the C^∞ mapping function Eq. (1):

$$(\alpha^1, \alpha^2, \alpha^3) \rightarrow (x^1(\alpha^1, \alpha^2, \alpha^3), x^2(\alpha^1, \alpha^2, \alpha^3), x^3(\alpha^1, \alpha^2, \alpha^3)) \tag{1}$$

where x^i are the standard components with respect to the Cartesian reference frame, and α^i instead are the general curvilinear coordinates [42]. A non-orthogonal local reference frame $(\mathbf{g}_1, \mathbf{g}_2, \mathbf{g}_3)$, tangential at the point $\mathbf{P}^{(0)}$ with respect to the curvilinear variables, is then introduced. The covariant base vectors in the reference configuration are defined as:

$$\mathbf{g}_i = \frac{\partial \boldsymbol{X}}{\partial \alpha^i} \qquad i = 1, 2, 3 \tag{2}$$

The vectors $\mathbf{g}_i$ can be, in general, non-unitary and non-orthogonal. The standard Cartesian reference frame, the covariant basis Eq. (2), and the geometrical description of an arbitrary curved body in the undeformed configuration are provided in Fig. 1.

Given these base vectors, the covariant and contravariant metric tensors are defined as:

$$g_{ij} = \mathbf{g}_i \cdot \mathbf{g}_j = \mathbf{g}_j \cdot \mathbf{g}_i = g_{ji} \tag{3}$$

$$g^{ik} g_{kj} = \delta^i_j \tag{4}$$

From these relations, the reciprocal dual basis, also called the contravariant basis, is computed as follows [43]:

$$\mathbf{g}^i = g^{ij} \mathbf{g}_j \tag{5}$$

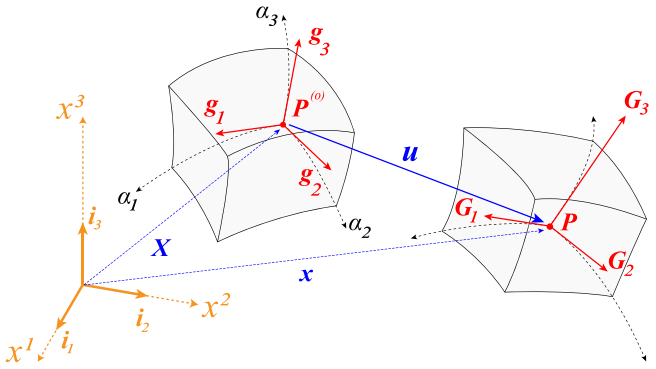

Fig. 1. Geometrical representation of undeformed and deformed configurations, with the global cartesian and local curvilinear reference frames in the material and actual configurations.

For further manipulations, the changes in the covariant and contravariant basis with respect to curvilinear coordinates are required. The derivatives of the bases are expressed in compact notation as:

$$(a): \frac{\partial \mathbf{g}_i}{\partial \alpha^j} = \Gamma^k_{ij}\mathbf{g}_k \qquad (b): \frac{\partial \mathbf{g}^i}{\partial \alpha^j} = -\Gamma^i_{kj}\mathbf{g}^k \tag{6}$$

where Γ^k_{ij} and Γ^i_{kj} are the Christoffel symbols, defined through the contravariant metric tensor and the derivative of the covariant metric tensor:

$$\Gamma^k_{ij} = \frac{1}{2}g^{kl}\left(\frac{\partial g_{il}}{\partial \alpha^j} + \frac{\partial g_{jl}}{\partial \alpha^i} - \frac{\partial g_{ij}}{\partial \alpha^l}\right) \tag{7}$$

In tensor calculus, the Christoffel symbols are strictly basis-dependent quantities and describe the variation of the curvilinear basis in space [44]. The same proposed procedure can be identically applied to derive the covariant and contravariant bases $\mathbf{G}_i$ and $\mathbf{G}^i$ in the actual deformed reference frame, considering the actual position vector $\boldsymbol{x}$, the co- and contravariant metric tensors G_{ij} and G^{ij} and the other related curvilinear quantities previously introduced [42].

Starting from these definitions, any vector field $\mathbf{u} : \boldsymbol{\Omega}_0 \rightarrow \mathbb{R}^3$ can be defined in the local co- and contravariant frame, and the differential operators are extended naturally by the extensive use of Christoffel symbols Eq. (6). If the vector field is defined with respect to the covariant basis, considering then $\mathbf{u} = u^i\mathbf{g}_i$, the partial derivative with respect to the generic α^j coordinate is naturally extended as:

$$\frac{\partial \mathbf{u}}{\partial \alpha^j} = \frac{\partial u^i}{\partial \alpha^j}\mathbf{g}_i + u^i\frac{\partial \mathbf{g}_i}{\partial \alpha^j} = \left(\frac{\partial u^i}{\partial \alpha^j} + u^k\Gamma^i_{kj}\right)\mathbf{g}_i = u^i|_j\mathbf{g}_i \tag{8}$$

The term $u^i_{|j}$ is the covariant derivative of the i-th component of the vector $\mathbf{u}$ with respect to the curvilinear variable α^j [44]. The same definition is exploited in the case of the contravariant basis, thus considering $\mathbf{u} = u_i\mathbf{g}^i$:

$$\frac{\partial \mathbf{u}}{\partial \alpha^j} = \frac{\partial u_i}{\partial \alpha^j}\mathbf{g}^i + u_i\frac{\partial \mathbf{g}^i}{\partial \alpha^j} = \left(\frac{\partial u_i}{\partial \alpha^j} + u_k\Gamma^k_{ij}\right)\mathbf{g}^i = u_i|_j\mathbf{g}^i \tag{9}$$

2.2. Kinematics description

Let $\chi : \boldsymbol{X} \in \boldsymbol{\Omega}_0 \rightarrow \boldsymbol{x} \in \boldsymbol{\Omega}$ be the mapping describing the motion of body from the undeformed $\boldsymbol{\Omega}_0$ configuration to the actual deformed $\boldsymbol{\Omega}$ configuration. In general, χ is a sufficiently smooth function taking into account physical compatibility conditions [42]. The Lagrangian displacement vector $\mathbf{u}$, expressed in the local curvilinear frames, is:

$$\mathbf{u} = \chi(\boldsymbol{X}) - \boldsymbol{X} = \boldsymbol{x} - \boldsymbol{X} = u_i\mathbf{g}^i = u^i\mathbf{g}_i \tag{10}$$

The kinematic descriptors of the body motion, namely the deformation gradient and the Green-Lagrange strain tensor, are derived following the classical continuum mechanics argument. Introducing the displacement gradient:

$$\nabla\mathbf{u} = \frac{\partial \mathbf{u}}{\partial \alpha^j} \otimes \mathbf{g}^j \tag{11}$$

The strain tensor is derived as:

$$\mathbf{E} = \frac{1}{2}\left(\nabla\mathbf{u} + (\nabla\mathbf{u})^T\right) = \frac{1}{2}\left(u_i|_j + u_j|_i\right)\mathbf{g}^i \otimes \mathbf{g}^j = \frac{1}{2}\left(\frac{\partial u_i}{\partial \alpha^j} + \frac{\partial u_j}{\partial \alpha^i} - 2u_k\Gamma^k_{ij}\right)\mathbf{g}^i \otimes \mathbf{g}^j$$
$$= \epsilon_{ij}\mathbf{g}^i \otimes \mathbf{g}^j \tag{12}$$

where ϵ_{ij} is the covariant strain component with respect to the curvilinear basis. In a finite element scenario, typically strain components are recovered in Cartesian coordinates, where the reference frame is fixed [45]. To perform the transformation of strain, consider again the Cartesian coordinates (x^1, x^2, x^3) and curvilinear covariant $(\alpha^1, \alpha^2, \alpha^3)$. In general, by the chain rule, one can define the following derivative operators:

$$(a): \frac{\partial(\cdot)}{\partial \alpha^j} = \frac{\partial(\cdot)}{\partial x^i}\cdot\frac{\partial x^i}{\partial \alpha^j}; \qquad (b): \frac{\partial(\cdot)}{\partial x^j} = \frac{\partial(\cdot)}{\partial \alpha^i}\cdot\frac{\partial \alpha^i}{\partial x^j}; \tag{13}$$

From these two differential operators, one can redefine the basis vectors and obtain the Jacobian between these two coordinate systems [45]:

$$\mathbf{g}_j = \frac{\partial \boldsymbol{X}}{\partial \alpha^j} = \frac{\partial \boldsymbol{X}}{\partial x^i}\cdot\frac{\partial x^i}{\partial \alpha^j} = \mathbf{i}_i\frac{\partial x^i}{\partial \alpha^j} \quad \rightarrow \quad \frac{\partial x^i}{\partial \alpha^j} = \mathbf{g}_j\cdot\mathbf{i}_i \tag{14}$$

$$\mathbf{i}_j = \frac{\partial \boldsymbol{X}}{\partial x^j} = \frac{\partial \boldsymbol{X}}{\partial \alpha^i}\cdot\frac{\partial \alpha^i}{\partial x^j} = \mathbf{g}_i\frac{\partial \alpha^i}{\partial x^j} \quad \rightarrow \quad \frac{\partial \alpha^i}{\partial x^j} = g^{ik}\left(\mathbf{g}_k\cdot\mathbf{i}_j\right) \tag{15}$$

Exploiting the change of variable introduced in Eq. (13), the relation between the covariant strain component ϵ_{ij} and the related Cartesian component strain component ϵ_{ij} is obtained [45]:

$$2\epsilon_{ij} = \frac{\partial \boldsymbol{x}}{\partial \alpha^i}\cdot\frac{\partial \boldsymbol{x}}{\partial \alpha^j} - \frac{\partial \boldsymbol{X}}{\partial \alpha^i}\cdot\frac{\partial \boldsymbol{X}}{\partial \alpha^j} = \left[\frac{\partial \boldsymbol{x}}{\partial x^k}\cdot\frac{\partial \boldsymbol{x}}{\partial x^l} - \frac{\partial \boldsymbol{X}}{\partial x^k}\cdot\frac{\partial \boldsymbol{X}}{\partial x^l}\right]\frac{\partial x^k}{\partial \alpha^i}\cdot\frac{\partial x^l}{\partial \alpha^j} = 2\epsilon_{kl}\frac{\partial x^k}{\partial \alpha^i}\cdot\frac{\partial x^l}{\partial \alpha^j} \tag{16}$$

In conclusion, the trasformation law between the reference frame Eq. (16) is then rewritten in compact form by considering Eq. (15):

$$\epsilon_{kl} = \frac{\partial \alpha^i}{\partial x^k}\frac{\partial \alpha^j}{\partial x^l}\epsilon_{ij} = g^{i\rho}g^{j\sigma}(\mathbf{g}_\rho\cdot\mathbf{i}_k)(\mathbf{g}_\sigma\cdot\mathbf{i}_l)\epsilon_{ij} = J^{ij}_{kl}\epsilon_{ij} \tag{17}$$

where $J^{ij}_{kl} = g^{i\rho}g^{j\sigma}(\mathbf{g}_\rho\cdot\mathbf{i}_k)(\mathbf{g}_\sigma\cdot\mathbf{i}_l)$ is the transformation matrix between the curvilinear and Cartesian reference frame, valid also for the stress tensor component [45].

3. 2|3D shell finite elements

3.1. CUF shell models

In the present section, the classical 2D CUF shell model is presented. An extensive description of this well-established model in the literature can be found in Carrera et al. [35]. Under the Unified formulation of 2D shell theories, implemented in the CUF formalism, the three-dimensional displacement field is provided as a recursive formal expression independent of the theory of structural approximation considered, which is effectively an input of the present model:

$$\mathbf{u}(\alpha^1, \alpha^2, \alpha^3) = F_\tau(\alpha^3)\mathbf{u}_\tau(\alpha^1, \alpha^2) \qquad \tau = 1, \dots, M+1 \tag{18}$$

where F_τ is the through-the-thickness polynomial expansion adopted, representing the theory of structural approximation adopted, M is the polynomial order of expansion, and $\mathbf{u}_\tau$ is the vector of generalized displacement components along the shell mid-surface. The choice of the through-the-thickness kinematics is uniquely represented by F_τ; in this

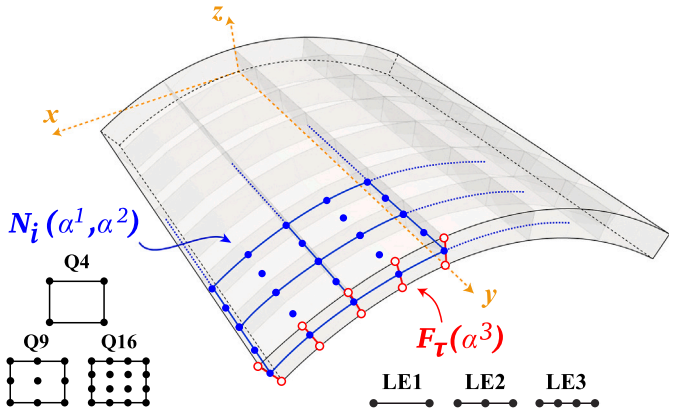

Fig. 2. Higher-order 2D CUF models.

way, any structural theory can be included in the displacement field model without any loss of generality. A graphical representation of classical 2D CUF models is proposed in Fig. 2.

Exploiting the Einstein notation for repeated subscript summation, any higher-order structural theory can be implemented automatically through the hierarchical nature of the displacement field definition. In this work, Lagrange expansion models (LE models) are exploited [35]. LE models are based on the use of Lagrange polynomials to interpolate the displacement field in the thickness direction α^3, with the possibility of discretizing the thickness into several local sub-domains. Thanks to this approach, local independent displacement fields can be defined for each sub-domain, assigning different expansion models independently from those of other components. For the sake of completeness, the displacement field of an LE2 parabolic expansion model is reported in Eq. (19):

$$\begin{cases} u_x(\alpha^1,\alpha^2,\alpha^3) = F_1(\alpha^3)u_{x_1}(\alpha^1,\alpha^2) + F_2(\alpha^3)u_{x_2}(\alpha^1,\alpha^2) + F_3(\alpha^3)u_{x_3}(\alpha^1,\alpha^2) \\ u_y(\alpha^1,\alpha^2,\alpha^3) = F_1(\alpha^3)u_{y_1}(\alpha^1,\alpha^2) + F_2(\alpha^3)u_{y_2}(\alpha^1,\alpha^2) + F_3(\alpha^3)u_{y_3}(\alpha^1,\alpha^2) \\ u_z(\alpha^1,\alpha^2,\alpha^3) = F_1(\alpha^3)u_{z_1}(\alpha^1,\alpha^2) + F_2(\alpha^3)u_{z_2}(\alpha^1,\alpha^2) + F_3(\alpha^3)u_{z_3}(\alpha^1,\alpha^2) \end{cases} \tag{19}$$

where $F_1(\alpha^3)$, $F_2(\alpha^3)$, and $F_3(\alpha^3)$ are parabolic Lagrange's polynomials defined over three nodes taken along the thickness. In the proposed case of LE2 expansion, such expansion basis is represented by:

$$N_1(\nu) = \frac{1}{2}(\nu^2 - \nu); \qquad N_2(\nu) = -\nu^2 + 1; \qquad N_3(\nu) = \frac{1}{2}(\nu^2 + \nu); \tag{20}$$

where ν is the natural coordinate describing the position along the thickness. The set of expansion basis functions is defined, as classically done, in the natural domain $\nu \in [-1;+1]$ to straightforwardly implement numerical procedures such as Gauss-Legendre quadrature rules and polynomial interpolation where the physical coordinates are reconstructed by means of the Jacobian, discussed later. The reader is addressed to Carrera et al. [35] for a complete description of the implementation of Lagrange Expansion theories (LE class) for all possible cases. Given the polynomial order adopted in the through-the-thickness expansion theory, the expansion models adopted will be referred to as linear LE1 (two-node), parabolic LE2 (three-node), and cubic LE3 model (four-node).

3.2. 2D finite element approximation

The continuous field of generalized unknowns on the shell mid-surface $\mathbf{u}_\tau(\alpha^1,\alpha^2)$ is then discretized following the classical FE approach, adopting 2D approximations:

$$\mathbf{u}_\tau(\alpha^1,\alpha^2) = N_i(\alpha^1,\alpha^2)\mathbf{u}_{\tau i} \qquad i = 1,\dots,N_n \tag{21}$$

where $N_i(x,y)$ are the 2D shape functions, N_n is the number of finite nodes adopted in the element formulation, and $\mathbf{u}_{\tau i}$, the final unknowns of the model, are the nodal displacement components.

In the present approach, the classical 2D FE formulations are adopted in the discretization of generalized unknowns, using the set of 2D Lagrange shape functions defined in the natural domain $(\xi,\eta) \in [-1;+1]\times[-1;+1]$. As an example, the shape functions adopted in the discretization of the mid-surface with a parabolic nine-node element are:

$$N_i(\xi,\eta) = \frac{1}{4}(\xi^2 + \xi\xi_i)(\eta^2 + \eta\eta_i), \qquad i = 1,3,5,7 \tag{22}$$

$$N_i(\xi,\eta) = \frac{1}{2}\xi_i^2(\xi^2 + \xi\xi_i)(1-\eta^2) + \frac{1}{2}\eta_i^2(\eta^2 + \eta\eta_i)(1-\xi^2), \qquad i = 2,4,6,8 \tag{23}$$

$$N_i(\xi,\eta) = (1-\xi^2)(1-\eta^2), \qquad i = 9 \tag{24}$$

where (ξ,η) are the natural coordinates and (ξ_i,η_i) are the natural coordinates of the interpolating nodes in the natural domain. More details about the 2D interpolation along the natural domain can be found in many works, see [1,35]. Given the total number of finite nodes adopted in the 2D element chosen, the discretization along the shell reference mid-surface will be addressed as linear Q4 (four-nodes), parabolic Q9 (nine-nodes), and cubic Q16 (sixteen-nodes) FE interpolation.

The final expression of the displacement field in the CUF domain is then a coupled expansion of the structural shell model and the FE approximation along the reference mid-surface, expressed through a single, unified, expression exploited by a recursive index notation:

$$\mathbf{u}(\alpha^1,\alpha^2,\alpha^3) = F_\tau(\alpha^3)\mathbf{u}_\tau(\alpha^1,\alpha^2) = F_\tau(\alpha^3)N_i(\alpha^1,\alpha^2)\mathbf{u}_{\tau i} \tag{25}$$

The final expression of the displacement field given in Eq. (25) is formally independent of the order of shell theory adopted and the mid-surface discretization. Any displacement-based model can be obtained hierarchically by choosing the two independent polynomial bases along the thickness and the midsurface. The reader is referred to [46] for additional insights about CUF shell models. In the literature, higher-order plate/shell models implemented in the CUF scenario have been proven effective in the computation of complex 3D stress and displacement distributions in various engineering fields, see [47–49].

3.3. CUF merged with FEM

Classical plate theories are not well-suited for modeling structures with variable thickness because the separation of functions $F_\tau(\alpha^3)$ and $N_i(\alpha^1,\alpha^2)$ presupposes that the geometry of the shell is orthogonal, that is the constant thickness of the shell through its mid-surface.

To overcome these challenges, non-conventional finite elements have recently been introduced, exploiting purely displacement-based formulations, capable of handling complex geometries without compromising the overall accuracy and computational efficiency of 1D and 2D models [50,51]. This approach, enabled by the CUF, is now extended for the first time to modeling structures in fully curvilinear coordinates for the analysis of shells with variable geometrical features. This extension allows for accurately representing complex shells within a unified 3D higher-order approximation. Furthermore, this approach exploits the use of different polynomial orders in different directions, enhancing the accuracy of the model while maintaining computational efficiency.

In the classical CUF approach, the approximating 2D shape functions of the shell mid-surface N_i and the thickness F_τ are treated separately throughout the derivation of FE governing equations. According to the node-dependent kinematic approach, later introduced by Li *et al.* [52], the coupling between these approximations is introduced by a recursive index formalism:

$$\mathbf{u}(\alpha^1,\alpha^2,\alpha^3) = F_\tau^i(\alpha^3)N_i(\alpha^1,\alpha^2)\mathbf{u}_{\tau i} \qquad \tau = 1,\dots,M^i+1; \qquad i = 1,\dots,N_n \tag{26}$$

Introducing the superscript "i" over the function F_τ in Eq. (26), a coupling between through-the-thickness kinematics and classical FE

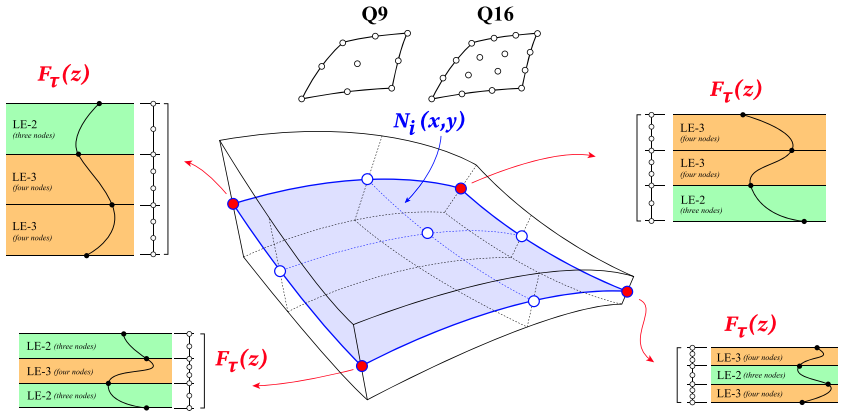

Fig. 3. Curvilinear finite element with a node-dependent approximation of through-the-thickness displacement field: geometrical representation of the shell with arbitrary curvature and variable thickness.

modeling of the mid-surface is definitively introduced; also, the number of expansion terms $M+1$ over the index τ now depends on the FE node i. In this sense, each finite node of the discretization can assume its own polynomial expansion in the thickness direction. The capabilities of the present approach have been established in many fields, both for 1D beam models [53–55] and 2D plate and shell models [52,56]. However, this approach is not yet able to describe a thickness variation across the midsurface of the shell element because the coordinates α^3 and (α^1, α^2) are handled separately in the approximation of both geometry and displacement fields during the derivation of governing equations.

In this work, the previous models are further improved by completely merging the functions $F_\tau^i(\alpha^3)$ and $N_i(\alpha^1, \alpha^2)$ into a unique 3D function $L_{\tau i}(\alpha^1, \alpha^2, \alpha^3)$ that, differently from classical 3D Lagrangian shape functions, can have different polynomial orders in α^3 direction and α^1, α^2 directions. Therefore, the displacement field can be rewritten as follows

$$\mathbf{u}(\alpha^1, \alpha^2, \alpha^3) = L_{\tau i}(\alpha^1, \alpha^2, \alpha^3)\mathbf{u}_{\tau i} \qquad \tau = 1, \dots, M^i + 1\,; \qquad i = 1, \dots, N_n \tag{27}$$

where $L_{\tau i}(\alpha^1, \alpha^2, \alpha^3) = F_\tau^i(\alpha^3)N_i(\alpha^1, \alpha^2)$. The new polynomial basis $L_{\tau i}$ can be interpreted as non-conventional 3D shape functions in which the order of expansion can be different along one of the spatial directions [50,51], in this case the thickness direction α^3.

From this point on, the governing equations are derived by using the above 3D approximation of the finite element domain. All the geometrical quantities, then all derivatives and integrals based on related transformation of coordinates, are computed as 3D, allowing us to consider the thickness variation inside the element itself. At the same time, this finite element does not add unknowns to the final system of equations because it employs the same identical variables as classical CUF shell models.

Note that, unlike classical 3D finite elements, the present elements do not suffer from numerical problems due to a possible high aspect ratio of the element; indeed, the use of a different order of expansion in the thickness direction with respect to the mid-surface directions automatically overcomes this problem. The study cases demonstrate this fact, as analyzed later.

A graphical representation of the finite element presented in this work is provided in Fig. 3.

4. Isoparametric formulation

In this section, the geometrical quantities previously introduced are now defined in the Unified framework exploiting the isoparametric formulation, namely adopting the same polynomial approximation for the displacement field and structural geometry [57]. The geometric reconstruction is fundamental in the definition of finite element matrices and the computation of strain and stress components in curvilinear coordinates.

4.1. Three-dimensional geometry interpolation

In the Cartesian reference frame with basis vectors $(\mathbf{i}_1, \mathbf{i}_2, \mathbf{i}_3)$, the position vector of a generic material point inside the discretized domain can be represented using curvilinear coordinates as:

$$\boldsymbol{X}(\alpha^1, \alpha^2, \alpha^3) = L_{\tau i}(\alpha^1, \alpha^2, \alpha^3)\boldsymbol{X}_{\tau i} \tag{28}$$

where $\boldsymbol{X}_{\tau i} = \{X^1_{\tau i}, X^2_{\tau i}, X^3_{\tau i}\}^T = \{X_{\tau i}, Y_{\tau i}, Z_{\tau i}\}^T$ is the vector of the physical coordinates of the $\tau - i$ discretized node. Unlike classical shell models, the present one does not introduce any linear assumption in the thickness direction α^3. Following the present definitions, the covariant basis vector is computed by Eq. (2):

$$\begin{cases} \mathbf{g}_1 = \frac{\partial L_{\tau i}}{\partial \alpha^1}\boldsymbol{X}_{\tau i} \\ \mathbf{g}_2 = \frac{\partial L_{\tau i}}{\partial \alpha^2}\boldsymbol{X}_{\tau i} \\ \mathbf{g}_3 = \frac{\partial L_{\tau i}}{\partial \alpha^3}\boldsymbol{X}_{\tau i} \end{cases} \tag{29}$$

Furthermore, the covariant metric tensor is computed by definition and rewritten in matrix form as:

$$[g_{ij}] = \mathbf{g}_i \cdot \mathbf{g}_j = \begin{bmatrix} (\mathbf{g}_1 \cdot \mathbf{g}_1) & (\mathbf{g}_1 \cdot \mathbf{g}_2) & (\mathbf{g}_1 \cdot \mathbf{g}_3) \\ (\mathbf{g}_2 \cdot \mathbf{g}_1) & (\mathbf{g}_2 \cdot \mathbf{g}_2) & (\mathbf{g}_2 \cdot \mathbf{g}_3) \\ (\mathbf{g}_3 \cdot \mathbf{g}_1) & (\mathbf{g}_3 \cdot \mathbf{g}_2) & (\mathbf{g}_3 \cdot \mathbf{g}_3) \end{bmatrix} \tag{30}$$

Subsequently, in matrix form, one naturally obtains the contravariant metric tensor by matrix inversion:

$$[g^{ij}] = [g_{ij}]^{-1} \tag{31}$$

The contravariant basis of the interpolated finite element domain is then obtained following Eq. (5):

$$\mathbf{g}^i = g^{ij}\mathbf{g}_j = \begin{cases} \mathbf{g}^1 = g^{11}\mathbf{g}_1 + g^{12}\mathbf{g}_2 + g^{13}\mathbf{g}_3 \\ \mathbf{g}^2 = g^{21}\mathbf{g}_1 + g^{22}\mathbf{g}_2 + g^{23}\mathbf{g}_3 \\ \mathbf{g}^3 = g^{31}\mathbf{g}_1 + g^{32}\mathbf{g}_2 + g^{33}\mathbf{g}_3 \end{cases} \tag{32}$$

Exploiting the superimposed geometry interpolation, one can automatically derive the Christoffel symbols by applying Eq. (6)(a):

$$\Gamma^c_{ab} = \mathbf{g}^c \cdot \frac{\partial g_a}{\partial \alpha^b} = \begin{bmatrix} \mathbf{g}^c \cdot \frac{\partial^2 L_{\tau i}}{\partial {\alpha^1}^2} \boldsymbol{X}_{\tau i} & \mathbf{g}^c \cdot \frac{\partial^2 L_{\tau i}}{\partial \alpha^1 \partial \alpha^2} \boldsymbol{X}_{\tau i} & \mathbf{g}^c \cdot \frac{\partial^2 L_{\tau i}}{\partial \alpha^1 \partial \alpha^3} \boldsymbol{X}_{\tau i} \\ \mathbf{g}^c \cdot \frac{\partial^2 L_{\tau i}}{\partial \alpha^2 \partial \alpha^1} \boldsymbol{X}_{\tau i} & \mathbf{g}^c \cdot \frac{\partial^2 L_{\tau i}}{\partial {\alpha^2}^2} \boldsymbol{X}_{\tau i} & \mathbf{g}^c \cdot \frac{\partial^2 L_{\tau i}}{\partial \alpha^2 \partial \alpha^3} \boldsymbol{X}_{\tau i} \\ \mathbf{g}^c \cdot \frac{\partial^2 L_{\tau i}}{\partial \alpha^3 \partial \alpha^1} \boldsymbol{X}_{\tau i} & \mathbf{g}^c \cdot \frac{\partial^2 L_{\tau i}}{\partial \alpha^3 \partial \alpha^2} \boldsymbol{X}_{\tau i} & \mathbf{g}^c \cdot \frac{\partial^2 L_{\tau i}}{\partial {\alpha^3}^2} N_i \boldsymbol{X}_{\tau i} \end{bmatrix}, \quad c = 1,2,3 \tag{33}$$

4.2. Displacement interpolation

The strain components given by Eq. (12) stem from the covariant derivative of the covariant components of the displacement field, Eq. (9). In the non-orthogonal coordinate system, the co- and contravariant basis vectors $\mathbf{g}_i$ and $\mathbf{g}^i$ are not unitary vectors in general; thus, to analyze strain and stress components in a displacement-based FE model it is useful to refer to the physical Cartesian components of displacements $\hat{u}_i$ instead of the tensor components u_i and u^i, as well as the strain components. The displacement field can be expressed in the Cartesian or covariant form as:

$$\hat{u}_k \mathbf{i}_k = u_j \mathbf{g}^j \tag{34}$$

The generic covariant component u_j in terms of the cartesian component $\hat{u}_k$ can be rewritten with algebra manipulation and exploiting the orthogonality between the co- and contravariant basis:

$$u_j = \hat{u}_k (\mathbf{g}^l)_k g_{jl} = \hat{u}_k (\mathbf{g}_j)_k = \hat{\mathbf{u}} \cdot \mathbf{g}_j \tag{35}$$

where $\hat{\mathbf{u}}$ is the displacement vector expressed in the Cartesian reference frame, and the symbol $(\cdot)_k$ stands for the k-th vector component. In this way, the covariant displacement component can be rewritten in matrix form as:

$$\begin{bmatrix} u_1 \\ u_2 \\ u_3 \end{bmatrix} = \begin{bmatrix} (\mathbf{g}_1)_1 & (\mathbf{g}_1)_2 & (\mathbf{g}_1)_3 \\ (\mathbf{g}_2)_1 & (\mathbf{g}_2)_2 & (\mathbf{g}_2)_3 \\ (\mathbf{g}_3)_1 & (\mathbf{g}_3)_2 & (\mathbf{g}_3)_3 \end{bmatrix} \begin{bmatrix} \hat{u}_1 \\ \hat{u}_2 \\ \hat{u}_3 \end{bmatrix} = \hat{u}_\lambda \mathbf{t}_\lambda \tag{36}$$

where the basis $\mathbf{t}_\lambda$ introduced here is given by the set of vectors:

$$\mathbf{t}_1 = \begin{bmatrix} (\mathbf{g}_1)_1 \\ (\mathbf{g}_2)_1 \\ (\mathbf{g}_3)_1 \end{bmatrix}; \quad \mathbf{t}_2 = \begin{bmatrix} (\mathbf{g}_1)_2 \\ (\mathbf{g}_2)_2 \\ (\mathbf{g}_3)_2 \end{bmatrix}; \quad \mathbf{t}_3 = \begin{bmatrix} (\mathbf{g}_1)_3 \\ (\mathbf{g}_2)_3 \\ (\mathbf{g}_3)_3 \end{bmatrix}; \tag{37}$$

and the cartesian components of the displacement vector are interpolated using the isoparametric formulation, following Eq. (26). Finally, the covariant derivative of the covariant component of the displacement field can be rewritten in terms of Cartesian physical components:

$$\begin{bmatrix} \frac{\partial u_1}{\partial \alpha^k} \\ \frac{\partial u_2}{\partial \alpha^k} \\ \frac{\partial u_3}{\partial \alpha^k} \end{bmatrix} = \frac{\partial \hat{u}_\lambda}{\partial \alpha^k} \mathbf{t}_\lambda + \hat{u}_\lambda \frac{\partial \mathbf{t}_\lambda}{\partial \alpha^k} \tag{38}$$

Let us focus on the matrix introduced in Eq. (36). It represents also the Jacobian matrix $\mathbf{J}$ of the element:

$$\mathbf{J} = \begin{bmatrix} (\mathbf{g}_1)_1 & (\mathbf{g}_1)_2 & (\mathbf{g}_1)_3 \\ (\mathbf{g}_2)_1 & (\mathbf{g}_2)_2 & (\mathbf{g}_2)_3 \\ (\mathbf{g}_3)_1 & (\mathbf{g}_3)_2 & (\mathbf{g}_3)_3 \end{bmatrix} \tag{39}$$

In classical shell formulations, the Jacobian of the midsurface is considered separately from the thickness Jacobian. In fact, the components $(\mathbf{g}_1)_3$, $(\mathbf{g}_2)_3$, $(\mathbf{g}_3)_1$ and $(\mathbf{g}_3)_2$ are null if the shell has constant thickness. In this work, the components above are computed to consider a possible thickness variation inside the shell element.

4.3. Curvilinear and Cartesian strain computation

In the present FE implementation, the symmetrical physical quantities, such as strain and stress fields, are rewritten in vector form, adopting Voigt's notation. Adopting this notation requires the definition of transformation matrices and derivative operators specifically for the symmetrization adopted. In the following section, all the physical quantities adopted in the derivation of FE matrices are presented, as well as the transformation law required for the computation of strain components in the Cartesian and curvilinear reference frames. Starting from the strain components Eq. (12), the strain vector is rewritten as follows:

$$\boldsymbol{\varepsilon}^{curv} = \begin{bmatrix} \varepsilon_{11} \\ \varepsilon_{22} \\ \varepsilon_{33} \\ \varepsilon_{13} \\ \varepsilon_{23} \\ \varepsilon_{33} \end{bmatrix} = \underbrace{\begin{bmatrix} \frac{\partial}{\partial \alpha^1} - \Gamma^1_{11} & -\Gamma^2_{11} & -\Gamma^3_{11} \\ -\Gamma^1_{22} & \frac{\partial}{\partial \alpha^2} - \Gamma^2_{22} & -\Gamma^3_{22} \\ -\Gamma^1_{33} & -\Gamma^2_{33} & \frac{\partial}{\partial \alpha^3} - \Gamma^3_{33} \\ \frac{\partial}{\partial \alpha^3} - 2\Gamma^1_{13} & -2\Gamma^2_{13} & \frac{\partial}{\partial \alpha^1} - 2\Gamma^3_{13} \\ -2\Gamma^1_{23} & \frac{\partial}{\partial \alpha^3} - 2\Gamma^2_{13} & \frac{\partial}{\partial \alpha^2} - 2\Gamma^3_{13} \\ \frac{\partial}{\partial \alpha^2} - 2\Gamma^1_{12} & \frac{\partial}{\partial \alpha^1} - 2\Gamma^2_{12} & -2\Gamma^2_{12} \end{bmatrix}}_{\mathbf{b}_{curv}} \begin{bmatrix} u_1 \\ u_2 \\ u_3 \end{bmatrix}$$
$$= \mathbf{b}_{curv} \begin{bmatrix} (\mathbf{g}_1)_1 & (\mathbf{g}_1)_2 & (\mathbf{g}_1)_3 \\ (\mathbf{g}_2)_1 & (\mathbf{g}_2)_2 & (\mathbf{g}_2)_3 \\ (\mathbf{g}_3)_1 & (\mathbf{g}_3)_2 & (\mathbf{g}_3)_3 \end{bmatrix} \begin{bmatrix} \hat{u}_1 \\ \hat{u}_2 \\ \hat{u}_3 \end{bmatrix} \tag{40}$$

where ε^{curv}_{ij} are the curvilinear strain components with respect to the dual $\mathbf{g}^i \otimes \mathbf{g}^j$ basis, and u_i are the covariant displacement components. If the curvilinear strains are written considering the Cartesian displacement components $\hat{u}_i$, they become:

$$\varepsilon^{curv}_{ij} = \mathbf{b}_{curv} \mathbf{J} \hat{\mathbf{u}} \tag{41}$$

Imposing now the 3D interpolation of the Cartesian strain components, one can automatically derive the interpolated curvilinear strain components from the Cartesian displacements $\hat{\mathbf{u}}_{\tau i} = (\hat{u}_{\tau i_x}, \hat{u}_{\tau i_y}, \hat{u}_{\tau i_z})^T$:

$$\boldsymbol{\varepsilon}^{curv} = \mathbf{b}_{curv} \begin{bmatrix} L_{\tau i}(\mathbf{g}_1)_1 & L_{\tau i}(\mathbf{g}_1)_2 & L_{\tau i}(\mathbf{g}_1)_3 \\ L_{\tau i}(\mathbf{g}_2)_1 & L_{\tau i}(\mathbf{g}_2)_2 & L_{\tau i}(\mathbf{g}_2)_3 \\ L_{\tau i}(\mathbf{g}_3)_1 & L_{\tau i}(\mathbf{g}_3)_2 & L_{\tau i}(\mathbf{g}_3)_3 \end{bmatrix} \begin{bmatrix} \hat{u}_{\tau i_x} \\ \hat{u}_{\tau i_y} \\ \hat{u}_{\tau i_z} \end{bmatrix}$$
$$= \mathbf{b}_{curv} \begin{bmatrix} L_{\tau i}(\mathbf{g}_1)_1 & L_{\tau i}(\mathbf{g}_1)_2 & L_{\tau i}(\mathbf{g}_1)_3 \\ L_{\tau i}(\mathbf{g}_2)_1 & L_{\tau i}(\mathbf{g}_2)_2 & L_{\tau i}(\mathbf{g}_2)_3 \\ L_{\tau i}(\mathbf{g}_3)_1 & L_{\tau i}(\mathbf{g}_3)_2 & L_{\tau i}(\mathbf{g}_3)_3 \end{bmatrix} \hat{\mathbf{u}}_{\tau i} \tag{42}$$

Applying the transformation law Eq. (17), the Cartesian strain components are automatically obtained, directly expressed in terms of Cartesian displacement components:

$$\boldsymbol{\varepsilon}^{cart} = \mathbf{J}_{c2c} \boldsymbol{\varepsilon}^{curv} = \mathbf{J}_{c2c} \mathbf{b}_{curv} \begin{bmatrix} L_{\tau i}(\mathbf{g}_1)_1 & L_{\tau i}(\mathbf{g}_1)_2 & L_{\tau i}(\mathbf{g}_1)_3 \\ L_{\tau i}(\mathbf{g}_2)_1 & L_{\tau i}(\mathbf{g}_2)_2 & L_{\tau i}(\mathbf{g}_2)_3 \\ L_{\tau i}(\mathbf{g}_3)_1 & L_{\tau i}(\mathbf{g}_3)_2 & L_{\tau i}(\mathbf{g}_3)_3 \end{bmatrix} \hat{\mathbf{u}}_{\tau i}$$
$$= \mathbf{J}_{c2c} \mathbf{B}^{\tau i}_{curv} \hat{\mathbf{u}}_{\tau i} \tag{43}$$

where $\mathbf{B}^{\tau i}_{curv}$ is the algebraic matrix of derivative operators applied to the displacement polynomial expansion, whose formal expression is provided in Appendix A, and $\mathbf{J}_{c2c}$ is the transformation matrix stemming from the transformation law, redefined in compact form to impose the Voigt's notation:

$$\mathbf{J}_{c2c} = \begin{bmatrix} g^{1\rho}(\mathbf{g}_\rho)_1\, g^{1\sigma}(\mathbf{g}_\sigma)_1 & g^{2\rho}(\mathbf{g}_\rho)_1\, g^{2\sigma}(\mathbf{g}_\sigma)_1 & g^{3\rho}(\mathbf{g}_\rho)_1\, g^{3\sigma}(\mathbf{g}_\sigma)_1 & (g^{1\sigma}(\mathbf{g}_\sigma)_1\, g^{3\rho}(\mathbf{g}_\rho)_1 + g^{1\rho}(\mathbf{g}_\rho)_1\, g^{3\sigma}(\mathbf{g}_\sigma)_1) & (g^{2\sigma}(\mathbf{g}_\sigma)_1\, g^{3\rho}(\mathbf{g}_\rho)_1 + g^{2\rho}(\mathbf{g}_\rho)_1\, g^{3\sigma}(\mathbf{g}_\sigma)_1) \\ g^{1\rho}(\mathbf{g}_\rho)_2\, g^{1\sigma}(\mathbf{g}_\sigma)_2 & g^{2\rho}(\mathbf{g}_\rho)_2\, g^{2\sigma}(\mathbf{g}_\sigma)_2 & g^{3\rho}(\mathbf{g}_\rho)_2\, g^{3\sigma}(\mathbf{g}_\sigma)_2 & (g^{1\sigma}(\mathbf{g}_\sigma)_2\, g^{3\rho}(\mathbf{g}_\rho)_2 + g^{1\rho}(\mathbf{g}_\rho)_2\, g^{3\sigma}(\mathbf{g}_\sigma)_2) & (g^{2\sigma}(\mathbf{g}_\sigma)_2\, g^{3\rho}(\mathbf{g}_\rho)_2 + g^{2\rho}(\mathbf{g}_\rho)_2\, g^{3\sigma}(\mathbf{g}_\sigma)_2) \\ g^{1\rho}(\mathbf{g}_\rho)_3\, g^{1\sigma}(\mathbf{g}_\sigma)_3 & g^{2\rho}(\mathbf{g}_\rho)_3\, g^{2\sigma}(\mathbf{g}_\sigma)_3 & g^{3\rho}(\mathbf{g}_\rho)_3\, g^{3\sigma}(\mathbf{g}_\sigma)_3 & (g^{1\sigma}(\mathbf{g}_\sigma)_3\, g^{3\rho}(\mathbf{g}_\rho)_3 + g^{1\rho}(\mathbf{g}_\rho)_3\, g^{3\sigma}(\mathbf{g}_\sigma)_3) & (g^{2\sigma}(\mathbf{g}_\sigma)_3\, g^{3\rho}(\mathbf{g}_\rho)_3 + g^{2\rho}(\mathbf{g}_\rho)_3\, g^{3\sigma}(\mathbf{g}_\sigma)_3) \\ g^{1\rho}(\mathbf{g}_\rho)_1\, g^{1\sigma}(\mathbf{g}_\sigma)_3 & g^{2\rho}(\mathbf{g}_\rho)_1\, g^{2\sigma}(\mathbf{g}_\sigma)_3 & g^{3\rho}(\mathbf{g}_\rho)_1\, g^{3\sigma}(\mathbf{g}_\sigma)_3 & (g^{1\sigma}(\mathbf{g}_\sigma)_3\, g^{3\rho}(\mathbf{g}_\rho)_1 + g^{1\rho}(\mathbf{g}_\rho)_1\, g^{3\sigma}(\mathbf{g}_\sigma)_3) & (g^{2\sigma}(\mathbf{g}_\sigma)_3\, g^{3\rho}(\mathbf{g}_\rho)_1 + g^{2\rho}(\mathbf{g}_\rho)_1\, g^{3\sigma}(\mathbf{g}_\sigma)_3) \\ g^{1\rho}(\mathbf{g}_\rho)_2\, g^{1\sigma}(\mathbf{g}_\sigma)_3 & g^{2\rho}(\mathbf{g}_\rho)_2\, g^{2\sigma}(\mathbf{g}_\sigma)_3 & g^{3\rho}(\mathbf{g}_\rho)_2\, g^{3\sigma}(\mathbf{g}_\sigma)_3 & (g^{1\sigma}(\mathbf{g}_\sigma)_3\, g^{3\rho}(\mathbf{g}_\rho)_2 + g^{1\rho}(\mathbf{g}_\rho)_2\, g^{3\sigma}(\mathbf{g}_\sigma)_3) & (g^{2\sigma}(\mathbf{g}_\sigma)_3\, g^{3\rho}(\mathbf{g}_\rho)_2 + g^{2\rho}(\mathbf{g}_\rho)_2\, g^{3\sigma}(\mathbf{g}_\sigma)_3) \\ g^{1\rho}(\mathbf{g}_\rho)_1\, g^{1\sigma}(\mathbf{g}_\sigma)_2 & g^{2\rho}(\mathbf{g}_\rho)_1\, g^{2\sigma}(\mathbf{g}_\sigma)_2 & g^{3\rho}(\mathbf{g}_\rho)_1\, g^{3\sigma}(\mathbf{g}_\sigma)_2 & (g^{1\sigma}(\mathbf{g}_\sigma)_2\, g^{3\rho}(\mathbf{g}_\rho)_1 + g^{1\rho}(\mathbf{g}_\rho)_1\, g^{3\sigma}(\mathbf{g}_\sigma)_2) & (g^{2\sigma}(\mathbf{g}_\sigma)_2\, g^{3\rho}(\mathbf{g}_\rho)_1 + g^{2\rho}(\mathbf{g}_\rho)_1\, g^{3\sigma}(\mathbf{g}_\sigma)_2) \end{bmatrix}$$

$$\times \begin{bmatrix} (g^{1\sigma}(\mathbf{g}_\sigma)_1\, g^{2\rho}(\mathbf{g}_\rho)_1 + g^{1\rho}(\mathbf{g}_\rho)_1\, g^{2\sigma}(\mathbf{g}_\sigma)_1) \\ (g^{1\sigma}(\mathbf{g}_\sigma)_2\, g^{2\rho}(\mathbf{g}_\rho)_2 + g^{1\rho}(\mathbf{g}_\rho)_2\, g^{2\sigma}(\mathbf{g}_\sigma)_2) \\ (g^{1\sigma}(\mathbf{g}_\sigma)_3\, g^{2\rho}(\mathbf{g}_\rho)_3 + g^{1\rho}(\mathbf{g}_\rho)_3\, g^{2\sigma}(\mathbf{g}_\sigma)_3) \\ (g^{1\sigma}(\mathbf{g}_\sigma)_3\, g^{2\rho}(\mathbf{g}_\rho)_1 + g^{1\rho}(\mathbf{g}_\rho)_1\, g^{2\sigma}(\mathbf{g}_\sigma)_3) \\ (g^{1\sigma}(\mathbf{g}_\sigma)_3\, g^{2\rho}(\mathbf{g}_\rho)_2 + g^{1\rho}(\mathbf{g}_\rho)_2\, g^{2\sigma}(\mathbf{g}_\sigma)_3) \\ (g^{1\sigma}(\mathbf{g}_\sigma)_2\, g^{2\rho}(\mathbf{g}_\rho)_1 + g^{1\rho}(\mathbf{g}_\rho)_1\, g^{2\sigma}(\mathbf{g}_\sigma)_2) \end{bmatrix} \tag{44}$$

In the present formulation, the formal expression of the algebraic matrix $\mathbf{B}^{\tau i}_{curv}$ is independent of the theory of structural approximation and the kinematic model adopted. Additionally, it is not dependent on the reference frame adopted in the FE definition since it is generally computed in the curvilinear reference frame, varying pointwise. The uniquely defined Cartesian components stem from the transformation law once the isoparametric formulation reconstructs the local covariant basis and the contra-contravariant metric tensor.

5. Governing equation

This section presents the numerical framework that has been developed, implementing the curvilinear finite element model discussed previously. The formulations of the static and free vibration problems are carried out within the classical continuum mechanics framework, and the governing equations are derived from variational principles. The equilibrium equations are then written in a compact matrix representation, thereby enabling the hierarchical implementation of the proposed displacement-based FE model independently of the finite element model adopted.

5.1. Principle of virtual displacement

The governing equations for the purely mechanical problem are exploited through the Principle of Virtual Displacements (PVD):

$$\delta\mathcal{L}_{int} + \delta\mathcal{L}_{ine} = \delta\mathcal{L}_{ext} \tag{45}$$

where $\delta\mathcal{L}_{int}$ is the virtual variation of internal strain energy stored during the deformation process, $\delta\mathcal{L}_{ext}$ is the virtual variation of the work of external loads done by virtual displacements and $\delta\mathcal{L}_{ine}$ is the virtual variation of the work done by inertia load, defined as:

$$\text{(a) } \delta\mathcal{L}_{int} = \int_{\Omega_0} \delta\boldsymbol{\epsilon}^{\mathrm{T}}\boldsymbol{\sigma}\, dV \quad \text{(b) } \delta\mathcal{L}_{ine} = \int_{\Omega_0} \delta\boldsymbol{u}^{\mathrm{T}}\rho\ddot{\mathbf{u}}\, dV \quad \text{(c) } \delta\mathcal{L}_{ext} = \int_{\Omega_0} \delta\boldsymbol{u}^{\mathrm{T}}\mathbf{f}\, dV \tag{46}$$

where $\boldsymbol{\epsilon}$ is the strain tensor, $\boldsymbol{\sigma}$ is the Cauchy's stress tensor, $\ddot{\mathbf{u}}$ is the acceleration vector, $\mathbf{f}$ is the vector of external loads, and the symbol δ denotes the virtual variation. In the present work, finite element models are defined in a Total Lagrangian (TL) approach; subsequently, all volume integrals are referred to the material (or reference) configuration.

For the FE implementation proposed, the virtual displacement and strain fields are written adopting the same polynomial expansion proposed in Eq. (28), following the isoparametric approach, adopting two different independent indices:

$$\delta\mathbf{u}(\alpha^1, \alpha^2, \alpha^3) = L_{sj}(\alpha^1, \alpha^2, \alpha^3)\delta\mathbf{u}_{sj} \tag{47}$$

In this way, the real and virtual strain fields are rewritten in compact form using the algebraic matrices of derivative operators applied to the 3D interpolating functions as shown previously by Eq. (43):

$$\boldsymbol{\epsilon} = \mathbf{J}_{c2c}\mathbf{B}^{\tau i}_{curv}\hat{\mathbf{u}}_{\tau i} \qquad \delta\boldsymbol{\epsilon} = \mathbf{J}_{c2c}\mathbf{B}^{sj}_{curv}\delta\hat{\mathbf{u}}_{sj} \tag{48}$$

5.2. Fundamental Nuclei

Starting from the definitions in Eq. (46), the energetic terms are rewritten in matrix form, expressed in terms of Fundamental Nuclei (FN), the basic elementary blocks of the present higher-order curvilinear FE models.

The internal strain energy contribution is then rewritten as:

$$\begin{aligned} \delta\mathcal{L}_{int} = \int_\Omega \delta\boldsymbol{\epsilon}^{\mathrm{T}}\boldsymbol{\sigma}\, dV &= \int_\Omega \delta\hat{\mathbf{u}}^T_{sj}\mathbf{B}^{sj\ T}_{curv}\mathbf{J}^T_{c2c}\mathbb{C}\mathbf{J}_{c2c}\mathbf{B}^{\tau i}_{curv}\hat{\mathbf{u}}_{\tau i}|\mathbf{J}|\, dV \\ &= \delta\hat{\mathbf{u}}^T_{sj}\left[\int_\Omega \mathbf{B}^{sj\ T}_{curv}\mathbf{J}^T_{c2c}\mathbb{C}\mathbf{J}_{c2c}\mathbf{B}^{\tau i}_{curv}|\mathbf{J}|\, dV\right]\hat{\mathbf{u}}_{\tau i} = \delta\hat{\mathbf{u}}^T_{sj}\mathbf{K}^{\tau sij}\hat{\mathbf{u}}_{\tau i} \end{aligned} \tag{49}$$

where $|\mathbf{J}|$ is the determinant of the Jacobian matrix used for the transformation of the integral over the volume. The matrix $\mathbf{K}^{\tau sij}$ is the 3×3 FN of the stiffness matrix. In the definition of stiffness matrix FN, the elasticity tensor $\mathbb{C}$ adopted is the classical 6×6 tensor expressed in the Cartesian reference frame, without any curvilinear representation, since all the physical quantities have been expressed in terms of Cartesian components.

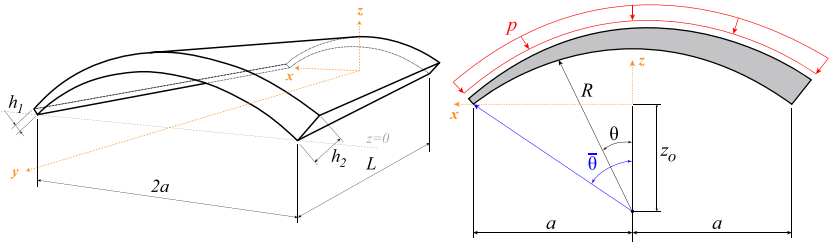

(a) Geometrical features (b) Boundary conditions

Fig. 4. Variable thickness shell: geometrical representation of the case study considered.

Referring to the inertial load contribution in the variational principle, instead:

$$\begin{aligned}\delta\mathcal{L}_{ine} &= \int_V \delta\boldsymbol{u}^{\mathrm{T}}\rho\ddot{\mathbf{u}}dV = \int_V \delta\hat{\mathbf{u}}_{sj}^T L_{sj}(\alpha^1,\alpha^2,\alpha^3)\ \rho\ L_{\tau i}(\alpha^1,\alpha^2,\alpha^3)\ddot{\hat{\mathbf{u}}}_{\tau i}|\mathbf{J}|\,dV \\ &= \delta\hat{\mathbf{u}}_{sj}^T\rho\left[\int_V L_{sj}(\alpha^1,\alpha^2,\alpha^3)\ \mathbf{I}\ L_{\tau i}(\alpha^1,\alpha^2,\alpha^3)|\mathbf{J}|\,dV\right]\ddot{\hat{\mathbf{u}}}_{\tau i} \\ &= \delta\hat{\mathbf{u}}_{sj}^T\mathbf{M}^{\tau sij}\ddot{\hat{\mathbf{u}}}_{\tau i} \end{aligned} \tag{50}$$

where ρ is the material density and $\mathbf{M}^{\tau sij}$ is the 3×3 FN of the mass matrix. Finally, considering the external load contribution in the variational principle, one can derive:

$$\begin{aligned}\delta\mathcal{L}_{ext} &= \int_\Sigma \delta\boldsymbol{u}^{\mathrm{T}}\mathbf{f}d\Sigma = \int_\Sigma \delta\hat{\mathbf{u}}_{sj}^T L_{sj}(\alpha^1,\alpha^2,\alpha_\Sigma^3)\mathbf{f}|\mathbf{J}_\Sigma|\,d\Sigma \\ &= \delta\hat{\mathbf{u}}_{sj}^T\left[\int_\Sigma \delta\hat{\mathbf{u}}_{sj}^T L_{sj}(\alpha^1,\alpha^2,\alpha_\Sigma^3)\mathbf{f}|\mathbf{J}_\Sigma|\,d\Sigma\right]\hat{\mathbf{u}}_{\tau i} = \delta\hat{\mathbf{u}}_{sj}^T\mathbf{P}^{sj}\end{aligned} \tag{51}$$

where a generic pressure load $\mathbf{f}(\alpha^1,\alpha^2) = \{f^1(\alpha^1,\alpha^2), f^2(\alpha^1,\alpha^2), f^3(\alpha^1,\alpha^2)\}^T$ is applied at $\alpha^3 = \alpha_\Sigma^3$ and $\mathbf{J}_\Sigma$ is the Jacobian computed at the same coordinate. The 3×1 vector $\mathbf{P}^{sj}$ is the FN of the vector of external loads.

Substituting the definition of virtual works in the PVD expression above, the governing equations for the purely mechanical problem are finally expressed in terms of FN:

$$\delta\hat{\mathbf{u}}_{sj}^T\mathbf{K}^{\tau sij}\hat{\mathbf{u}}_{\tau i} + \delta\hat{\mathbf{u}}_{sj}^T\mathbf{M}^{\tau sij}\ddot{\hat{\mathbf{u}}}_{\tau i} = \delta\hat{\mathbf{u}}_{sj}^T\mathbf{P}^{sj} \tag{52}$$

After the summation over indices τ, s, i and j and considering the CUF assembling procedure [35], the global stiffness matrix $\mathbf{K}$, the mass matrix $\mathbf{M}$ and external load vector $\mathbf{P}$ are obtained, and the final governing equations are written in the classical form:

$$\text{Static analysis: } \mathbf{Ku} = \mathbf{P} \tag{53}$$

$$\text{Modal analysis: } (\mathbf{K} - \omega^2\mathbf{M})\mathbf{\Phi} = 0 \tag{54}$$

In a CUF-based finite element model, as shown here, the governing equations are expressed using FN, matrices independent of the specific structural theory, such as the thickness expansion functions (F_τ and F_s) or mid-surface kinematic models (N_i and N_j). This invariance allows for the flexible implementation of various structural theories without limitations. The core advantage of the CUF approach is its ability to derive governing equations independent of the chosen FE implementation models. In particular, the use of Lagrange's expansion models (LE models) ensures the C_z^0 through-the-thickness requirements [58]. The final form of the FN and the hierarchical nature of these basic building blocks allow a straightforward implementation of node-dependent kinematic (NDK) models by considering different through-the-thickness expansion models and local refinements, guaranteeing accuracy, feasibility, and reduced computational costs with respect to full 3D finite element models with classical formulation (brick models). To assess the capabilities of the present displacement-based curvilinear CUF models, the classical linear stress analysis (static analysis) and free vibration analysis (modal analysis) of isotropic, variable-thickness, and variable-curvature structures are discussed.

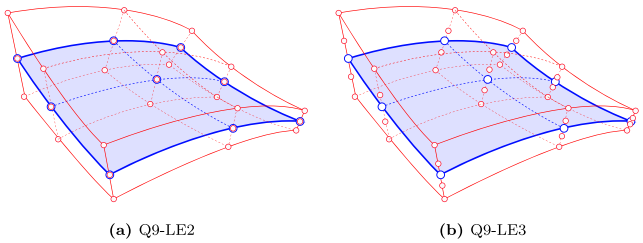

(a) Q9-LE2 (b) Q9-LE3

Fig. 5. Variable thickness shell: node-dependent kinematic curvilinear model adopted in the mathematical modeling of geometry and displacement field.

6. Numerical results

This section presents the proposed case studies and numerical results for the static and modal analysis of shells with variable thickness and arbitrary curvature. The analyses are performed using the present implementation of higher-order curvilinear models exploiting the NDK approach, which enhances the representation of structures with spatially varying curvature and thickness. The results are compared against reference solutions obtained using the conventional 3D finite element implementation in ABAQUS. The effectiveness of the proposed approach will be assessed through different case studies, demonstrating its capability and accuracy in different problems.

6.1. Variable thickness curved panel

The first case study analyzed is the static and modal analysis of a curved panel with variable thickness. The present analysis is proposed to assess the capabilities and the accuracy of the present model when a constant curvature and variable-thickness structure are considered. Specifically, a curved panel of total lateral length L = 100 cm and half-opening width $a = 20$ cm is analyzed. For the sake of convenience, the base points of the geometry are lying in the (x, y) plane. The constant radius of curvature of the inner surface is then fixed obtained by considering the center in the (x, z) plane at coordinates $(x_O, z_O) = (0, -25)$ cm, obtaining then $R = \sqrt{z_O^2 + a^2}$. To impose a thickness variation law, the angle θ is introduced, which can vary between $[-\bar{\theta}; +\bar{\theta}]$, where $\bar{\theta} = \arctan(a/z_O)$. In the considered case, the curved panel has a variable thickness in the tangential direction, ranging from $h_1 = 1$ cm to $h_2 = 4$ cm, with a linear variation law described by:

$$h(\theta) = h_1 + \frac{\theta + \bar{\theta}}{2\bar{\theta}}(h_2 - h_1) \quad \theta \in [-\bar{\theta}, +\bar{\theta}] \tag{55}$$

The curved panel is made of steel, for which the material properties considered are expressed in terms of Young's modulus $E = 210$ GPa and

Poisson's ratio $\nu = 0.3$. The structure is subjected to a uniform normal pressure and is considered clamped at one end. The geometrical features are depicted in Fig. 4(a), whereas the boundary conditions and the applied load are shown in Fig. 4(b).

In the present case, different mathematical models are considered in the discretization of the structure, and the geometry is considered to analyze the influence of different polynomial orders of expansion along the reference mid-surface and along the thickness. The results obtained with the present implementation of curvilinear NDK models are compared with reference solutions computed adopting classical 3D discretization implemented in the commercial software ABAQUS. The influence of different discretizations on the accuracy and the total computational cost required by the simulation is measured by comparing the relative percentage difference $\frac{(\cdot)\text{2D CUF}-(\cdot)\text{3D}}{(\cdot)\text{3D}} \cdot 100\ \%$ and the total degrees of freedom (DOF) of the model.

In the following analyses, two different FE formulations will be considered, analyzing the influence of parabolic and cubic polynomial expansion along different directions on the static and modal response of the structure. The graphical representation of the mathematical model adopted in the following discretization is depicted in Fig. 5. A convergence analysis is performed to assess the accuracy and efficiency of the 2|3D shell models regarding natural frequencies, considering the geometrical features described before. The influence of the mathematical models adopted on the natural frequencies is investigated considering only parabolic Q9 elements along the reference mid-surface, assessing the influence of the finite element mesh and the through-the-thickness discretization model (parabolic LE2 model or cubic LE3 model) initially.

The results of higher-order curvilinear 2D CUF elements are extensively compared with the natural frequencies obtained via numerical simulation of the 3D ABAQUS model, for which 9000 C3D20 elements (parabolic 20-node brick elements) are employed, due to hexahedral models' aspect ratio constraints. Table 1 shows the results of the modal analysis, performed to evaluate the influence of the reference mid-surface discretization and theory of structure approximation on the first ten natural frequencies of the clamped curved panel. Accurate results are obtained using coarser discretization, for each expansion model considered. Therefore, from now on, finite element mesh of at least 20×20 elements will be employed in further analysis. In particular, by considering the fixed total number of elements adopted in the reference surface, the adoption of cubic models leads to similar results in terms of natural frequencies. In all the cases, a significant reduction of the total computational cost in DOF is observed for all the discretization models adopted, compared to the convergent mesh adopted in the full 3D ABAQUS model.

Fig. 6 shows the through-the-thickness transversal displacement u_z distribution of the clamped plate when a normal pressure applied of $p = 10\ \text{N/cm}^2$ is considered. The results are compared at the position located at $\theta = 0$ and $y = 20$ cm from the clamped section. From the proposed results, the distribution of the through-the-thickness displacement shows a slight parabolic behavior, and more accurate results are observed when fine mesh along the reference surface is considered. Moreover, considering the fixed number of elements adopted in the discretization, slightly different solutions are observed when considering higher-order expansion models. The differences in the displacement distributions across

Table 1
Variable thickness curved panel: convergence analysis on natural frequencies [Hz]. Comparison between 2D CUF curvilinear models and 3D elasticity solutions. In brackets, the percentage difference of the proposed solutions.

Mode	Parabolic expansion model (LE2)				Cubic expansion model (LE3)				ABQ 3D
	10×10 Q9	15×15 Q9	20×20 Q9	20×30 Q9	10×10 Q9	15×15 Q9	20×20 Q9	20×30 Q9	C3D20
1	64.44(0.91 %)	64.27(0.65 %)	64.20(0.53 %)	64.14(0.43 %)	64.43(0.89 %)	64.27(0.63 %)	64.19(0.52 %)	64.13(0.42 %)	63.86
2	122.32(0.44 %)	121.88(0.09 %)	121.73(−0.04 %)	121.65(−0.11 %)	121.91(0.10 %)	121.49(0.24 %)	121.34(0.36 %)	121.26(0.43 %)	121.78
3	324.28(0.95 %)	323.60(0.73 %)	323.28(0.64 %)	323.01(0.55 %)	324.26(0.94 %)	323.57(0.73 %)	323.25(0.63 %)	322.98(0.54 %)	321.24
4	352.33(0.82 %)	351.03(0.45 %)	350.58(0.32 %)	350.23(0.22 %)	352.05(0.74 %)	350.76(0.37 %)	350.31(0.24 %)	349.96(0.14 %)	349.46
5	372.48(0.30 %)	370.83(−0.14 %)	370.29(−0.29 %)	369.94(−0.38 %)	371.82(0.12 %)	370.19(0.32 %)	369.65(0.46 %)	369.31(0.56 %)	371.37
6	645.16(0.76 %)	640.20(−0.02 %)	638.69(−0.25 %)	637.81(−0.39 %)	644.49(0.65 %)	639.54(0.12 %)	638.04(0.36 %)	637.16(0.49 %)	640.32
7	696.76(0.62 %)	694.05(1.01 %)	693.48(1.09 %)	693.39(1.10 %)	695.73(0.77 %)	693.09(1.14 %)	692.54(1.22 %)	692.45(1.24 %)	701.11
8	818.75(1.03 %)	813.56(0.39 %)	812.12(0.21 %)	811.28(0.10 %)	816.78(0.78 %)	811.71(0.16 %)	810.29(0.02 %)	809.45(0.12 %)	810.43
9	905.27(0.56 %)	900.22(0.00 %)	898.75(0.17 %)	898.05(0.25 %)	903.15(0.32 %)	898.22(0.23 %)	896.80(0.38 %)	896.13(0.46 %)	900.26
10	947.65(2.22 %)	934.29(0.78 %)	930.45(0.36 %)	928.39(0.14 %)	946.57(2.10 %)	933.20(0.66 %)	929.40(0.25 %)	927.36(0.03 %)	927.08
DOF	3969	8649	15,129	22,509	5292	11,532	20,172	30,012	151,995

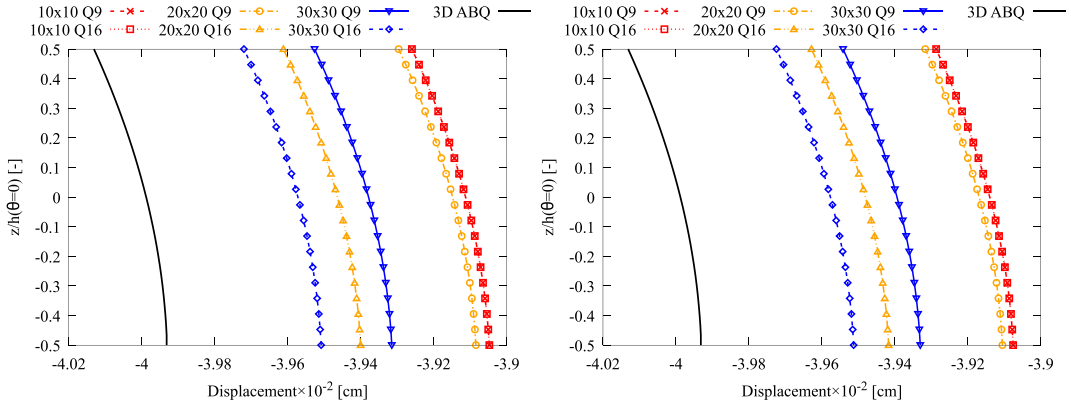

(a) Parabolic LE2 exp. model (b) Cubic LE3 exp. model

Fig. 6. Variable thickness curved panel: through-the-thickness displacement distribution of the clamped panel for different discretization models adopted. Results computed at $\theta = 0$ and $y = 20$ cm from the clamped section. Influence of the finite element mesh and expansion model adopted on the displacement distribution.

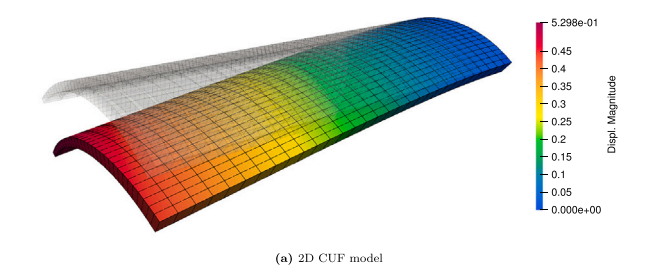

(a) 2D CUF model

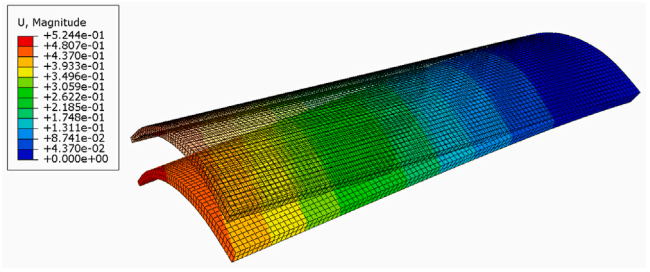

(b) 3D ABQ model

Fig. 7. Variable thickness curved panel: plot of the global displacement magnitude, comparison between 30×30 Q9 + 1LE2 model and 9000 C3D20 ABAQUS model.

parabolic LE2 and cubic LE3 models are almost negligible. Instead, a strong influence of the reference mid-surface discretization adopted is observed, and the most accurate results are observed when 30×30 FE are adopted. Fig. 7 shows the comparison of the displacement magnitude contour, comparing the solutions obtained via CUF model and ABAQUS model.

Fig. 8 shows the through-the-thickness distribution of the Cartesian strain component in the three normal directions ϵ_{xx}, ϵ_{yy} and ϵ_{zz}. In the following results, strain components are analyzed to assess the capabilities of the present implementation of the curvilinear model to accurately predict the three-dimensional strain field starting from a polynomial approximation of the local co- and contravariant basis and metric tensors from the geometric interpolation since they are required from Eq. (43). In this sense, this proposed case study investigates the performance of the present model where a non geometrically exact curvilinear model is considered. From the proposed results, the through-the-thickness strain ϵ_{xx} distribution shows some discrepancies with the reference 3D solution, but comparable and consistent results are obtained when refined meshes are considered. Instead, in the case of ϵ_{yy} and ϵ_{zz}, perfectly matching distributions across all the discretizations investigated.

6.2. Variable thickness and variable curvature structure

The proposed approach is exploited in the following case studies to model variable curvature and variable thickness structures. For this purpose, the analysis of isotropic variable curvature revolution structures is investigated. In the following, two different structures will be analyzed: a single curvature variation with a single thickness variation is considered; afterward, a single curvature variation and a double thickness variation are considered.

6.2.1. Generation of variable curvature and thickness structures

A reference surface of revolution is considered in generating the 3D model. The reference geometry adopted in the following is represented in Fig. 9(a). A general curved 2D reference mid-surface is considered in the 3D space, obtained by the revolution around the z axis of a variable curvature line on the $y-z$ plane. Given the initial radius of curvature in the $x-y$ plane denoted by R_0, the generic $R(\Psi)$ is obtained by rotating the reference radius of an angle Ψ with respect to the y axis with modulus expressed by the law $R(\Psi) = R_0 \cdot f(\Psi)$. Fig. 9(b) shows the graphical representation of the revolved 2D reference surface and its geometrical parameters adopted. Due to the symmetries of the structure, it is possible to analyze only an eighth of the global model considered.

Given the 3D reference surface, it is possible to compute locally the local covariant reference frame ($\mathbf{g}_1, \mathbf{g}_2$ vectors, instead the local $\mathbf{g}_3$ vector is always considered in the local normal direction. The thickness expansion will be considered along the $\mathbf{g}_3$ local direction). Given the opening angle denoted with Ψ_{op}, the local thickness of the structure is computed, in the proposed case studies, with a linear variation law in the $\mathbf{g}_2$ direction:

$$h_{\mathbf{g}_3}(\Psi) = h_1 + \frac{\Psi}{\Psi_{op}}(h_2 - h_1) \quad \Psi \in [0, \Psi_{op}] \tag{56}$$

Naturally, in the proposed approach, any thickness variation law can be straightforwardly implemented in the model since the 3D geometrical reconstruction is considered inside the computation of FE matrices. In this way, variable thickness geometries are straightforwardly obtained by uniquely assigning the two mathematical expressions for the thickness expansion and the radius law. In particular, in the following case studies, thick-to-thin structures will be analyzed to assess the capabilities of the present modeling technique. Moreover, the next case studies will consider two different radius laws. The expressions adopted and the geometrical parameters of the 3D geometries are listed in Table 2. In the case of cosine radius law, a single thickness variation along the $\mathbf{g}_2$ direction will be considered. Thereafter, for the case of the secant radius law, two different thickness variations will be considered in $\mathbf{g}_2$ and $\mathbf{g}_1$ directions.

6.2.2. Double curvature and single thickness variation

In the first case, the spherical-like curved structure with radius law $R(\Psi) = R_0 \cos^2(\Psi)$ is analyzed. The structure is made again of steel; the material constants considered are Young's modulus $E = 210$ GPa, Poisson's ratio $\nu = 0.33$, and density $\rho = 7850$ kg/m^3. Fig. 10(a) shows a representative discretization of the reference mid-surface obtained by the procedure described before.

The first analysis considered is the assessment of the capabilities of the present approach by convergence analysis on the first ten natural frequencies. In this preliminary analysis, only parabolic Q9 (nine-node) discretizations are adopted in the reference mid-surface model, considering different CUF LE models for the through-the-thickness expansion along the $\mathbf{g}_3$ direction instead. The natural frequencies obtained via higher-order 2D curvilinear CUF elements are compared with a reference solution computed by a full 3D ABAQUS model, in which 12740 C3D20 hexahedral elements (20-node bi-quadratic 3D elements) are adopted.

Table 3 shows the first five natural frequencies of the spherical-like structure, analyzing again the influence of theory of structure approximation and FE reference mid-surface discretization on the structural modal behavior, comparing extensively the proposed results obtained with curvilinear 2|3D models and reference 3D ABAQUS models. As done in the previous case study, the computational cost is measured in total DOF and the relative percentage difference is reported in brackets. Fig. 11 shows the first five normal modes of vibrations, plotting the eigenvectors computed by the numerical simulation adopting the 20×20 Q9 + 1LE3 CUF model. The proposed results show that for coarser discretization where 10×10 FE along the reference mid-surface the predictions in terms of natural frequencies are affected by more evident relative errors, attributed to the computation of local co- and contravariant bases within larger elements, that are not able to capture accurately the geometrical feature variations due to their dimensions. Instead, adopting 20×20 FE mesh increases the accuracy in terms of natural frequencies, observing also perfectly matching solutions in the case of 40×40 FE.

Discrepancies are found in the case of 30×30 FE results, attributed to the nodes distribution within the curved domain and the effect of geometry variation. However, relatively small percentage difference with

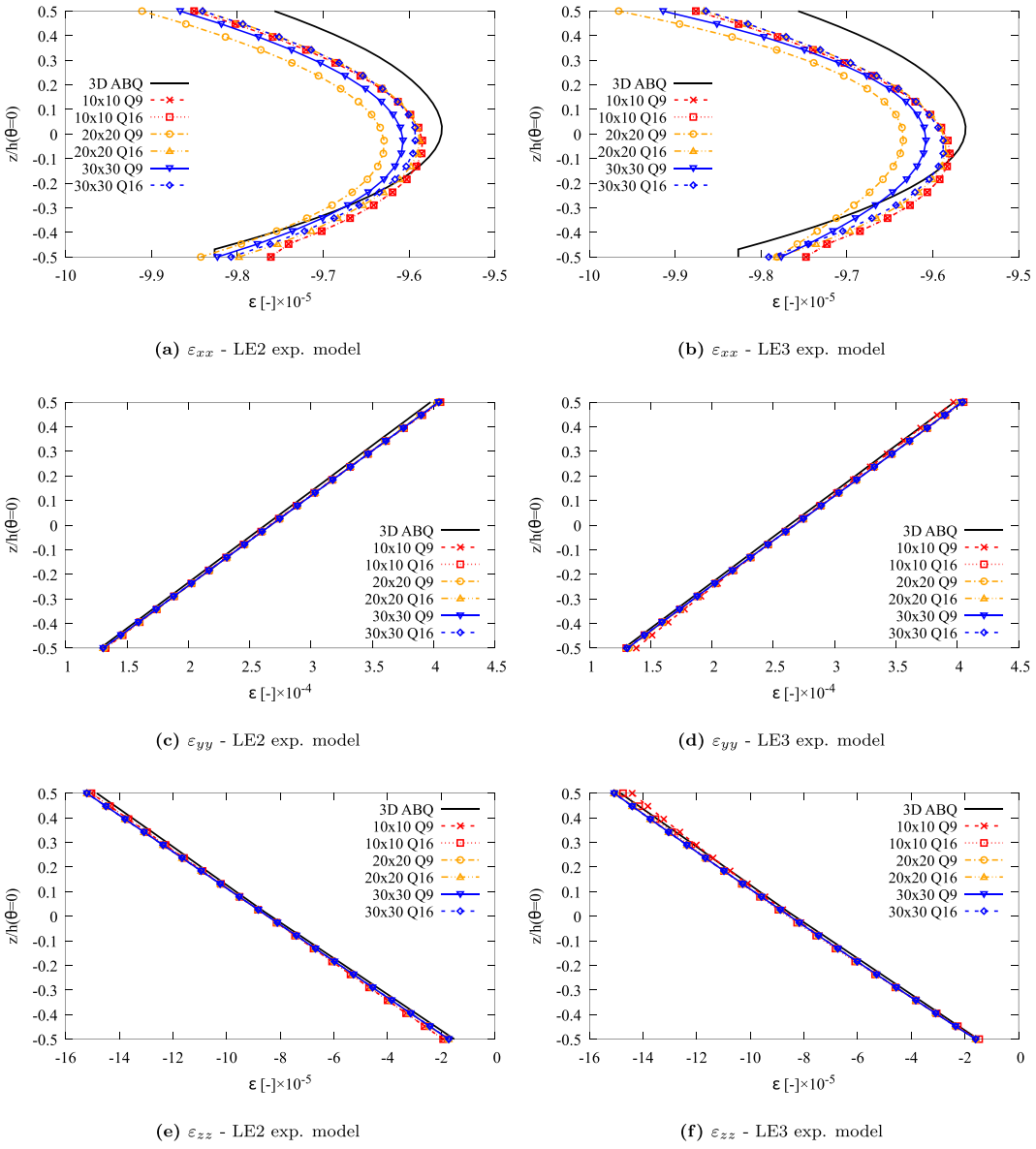

(a) ε_{xx} - LE2 exp. model (b) ε_{xx} - LE3 exp. model

(c) ε_{yy} - LE2 exp. model (d) ε_{yy} - LE3 exp. model

(e) ε_{zz} - LE2 exp. model (f) ε_{zz} - LE3 exp. model

Fig. 8. Variable thickness curved panel: through-the-thickness cartesian strain component distribution of the clamped panel for different discretization models adopted. Results computed at $\theta = 0$ and $y = 20$ cm from the clamped section. Influence of the finite element mesh and expansion model adopted on the strain distribution.

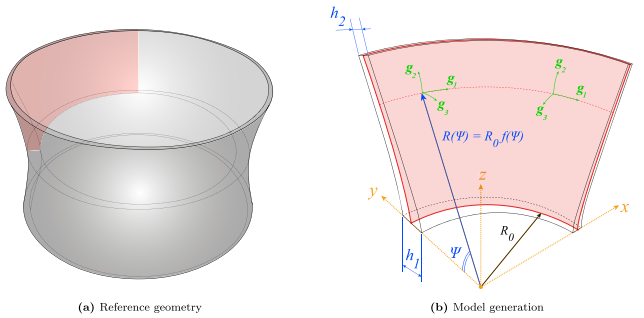

(a) Reference geometry (b) Model generation

Fig. 9. Variable thickness and curvature structures: model generation and the physical parameters adopted.

respect to the reference solution is still observed. Afterwards, the linear static analysis of the same structure is performed, considering symmetric boundary conditions and the application of a constant internal normal pressure, applied in $\mathbf{g}_3$ local direction, with an amplitude of $p = 1$ MPa. Fig. 10(b) depicts the boundary conditions and the load applied. The results obtained with higher-order 2D curvilinear CUF models are compared with the ABAQUS commercial software's reference 3D elasticity solution. In the following, the influence of the mathematical model adopted in the structure discretization is analyzed by comparing the through-the-thickness distribution of Cartesian displacements and stress components, analyzed at the $y = 0$ symmetry section in correspondence with the $x - y$ symmetry plane, namely along the line given by the A-B point represented in Fig. 10(b).

Table 2
Variable thickness and curvature structures: catenary and cosine radius law, geometrical parameters adopted.

Radius law	Range of Ψ	R_0 [m]	h_1 [m]	h_2 [m]
$f(\Psi) = \sec^2(\Psi)$	$[0; 30°]$	1	0.15	0.05
$f(\Psi) = \cos^2(\Psi)$	$[0; 60°]$	1	0.15	0.05

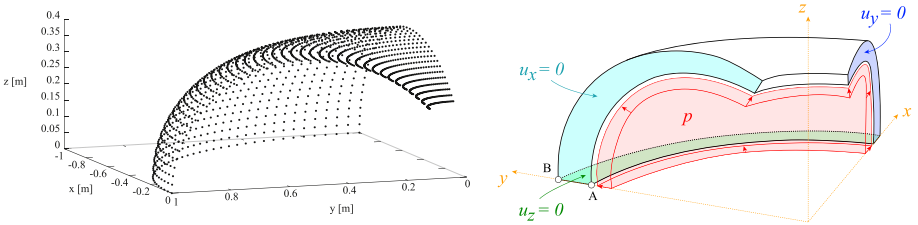

(a) Reference mid-surface discretization (b) Boundary conditions

Fig. 10. Variable thickness and curvature structures, cosine radius law structure $R(\Psi) = R_0 \cos^2(\Psi)$: geometrical features and boundary conditions considered.

Table 3
Variable thickness and curvature structures, spherical-like curved structure $R(\Psi) = R_0 \cos^2(\Psi)$: first five natural frequencies, comparison between curvilinear 2D CUF models' results and 3D ABAQUS solution. Frequencies measured in [Hz].

Mesh	Exp. model	Mode 1	Mode 2	Mode 3	Mode 4	Mode 5	DOF
10 × 10 Q9	1 LE2	403.67$^{(3.66\ \%)}$	535.85$^{(-5.06\ \%)}$	776.25$^{(-7.66\ \%)}$	819.68$^{(-3.54\ \%)}$	1148.65$^{(-4.94\ \%)}$	3969
	1 LE3	404.55$^{(3.89\ \%)}$	535.93$^{(-5.05\ \%)}$	856.39$^{(1.88\ \%)}$	863.33$^{(1.60\ \%)}$	1216.21$^{(0.65\ \%)}$	8649
	2 LE2	400.95$^{(2.96\ \%)}$	532.83$^{(-5.60\ \%)}$	770.21$^{(-8.37\ \%)}$	812.42$^{(-4.39\ \%)}$	1133.05$^{(-6.24\ \%)}$	6615
	2 LE3	403.13$^{(3.52\ \%)}$	534.63$^{(-5.28\ \%)}$	838.65$^{(-0.23\ \%)}$	850.09$^{(0.04\ \%)}$	1196.11$^{(-1.02\ \%)}$	9261
20 × 20 Q9	1 LE2	390.16$^{(0.19\ \%)}$	564.68$^{(0.05\ \%)}$	851.50$^{(1.30\ \%)}$	842.72$^{(0.82\ \%)}$	1215.46$^{(0.58\ \%)}$	15,129
	1 LE3	389.43$^{(0.01\ \%)}$	564.32$^{(0.02\ \%)}$	840.88$^{(0.03\ \%)}$	849.66$^{(0.01\ \%)}$	1208.93$^{(0.04\ \%)}$	20,172
	2 LE2	389.48$^{(0.02\ \%)}$	564.34$^{(0.01\ \%)}$	840.99$^{(0.05\ \%)}$	849.76$^{(0.00\ \%)}$	1209.32$^{(0.08\ \%)}$	25,215
	2 LE3	389.42$^{(0.00\ \%)}$	564.31$^{(0.02\ \%)}$	840.86$^{(0.03\ \%)}$	849.62$^{(0.01\ \%)}$	1208.82$^{(0.03\ \%)}$	35,301
30 × 30 Q9	1 LE2	394.34$^{(1.27\ \%)}$	553.14$^{(2.00\ \%)}$	858.21$^{(2.10\ \%)}$	855.45$^{(0.67\ \%)}$	1220.12$^{(0.97\ \%)}$	33,489
	1 LE3	393.40$^{(1.02\ \%)}$	552.94$^{(2.03\ \%)}$	855.29$^{(1.75\ \%)}$	851.48$^{(0.21\ \%)}$	1210.28$^{(0.16\ \%)}$	44,652
	2 LE2	393.12$^{(0.95\ \%)}$	551.57$^{(2.28\ \%)}$	854.71$^{(1.68\ \%)}$	850.44$^{(0.08\ \%)}$	1209.06$^{(0.05\ \%)}$	55,815
	2 LE3	392.84$^{(0.88\ \%)}$	551.45$^{(2.30\ \%)}$	847.76$^{(0.85\ \%)}$	853.28$^{(0.42\ \%)}$	1206.62$^{(0.15\ \%)}$	78,141
40 × 40 Q9	1 LE2	390.12$^{(0.18\ \%)}$	564.63$^{(0.04\ \%)}$	842.65$^{(0.24\ \%)}$	851.43$^{(0.20\ \%)}$	1214.95$^{(0.54\ \%)}$	59,049
	1 LE3	389.40$^{(0.00\ \%)}$	564.27$^{(0.02\ \%)}$	840.81$^{(0.02\ \%)}$	849.59$^{(0.02\ \%)}$	1208.46$^{(0.01\ \%)}$	78,732
	2 LE2	389.44$^{(0.01\ \%)}$	564.29$^{(0.02\ \%)}$	840.92$^{(0.04\ \%)}$	849.69$^{(0.00\ \%)}$	1208.84$^{(0.04\ \%)}$	98,415
	2 LE3	389.39$^{(0.01\ \%)}$	564.27$^{(0.02\ \%)}$	840.78$^{(0.02\ \%)}$	849.55$^{(0.02\ \%)}$	1208.34$^{(0.00\ \%)}$	137,781
ABQ	C3D20	389.41	564.41	840.60	849.73	1208.40	180,996

Fig. 12 shows the through-the-thickness transversal displacement distribution, which is given by the u_x component, for different discretization models along the reference mid-surface and CUF expansion models. Fig. 12(a) shows the displacement distribution when 20×20 FE are adopted in the reference mid-surface discretization, adopting both parabolic Q9 and cubic Q16 2D elements. A similar comparison is proposed in Fig. 12(b) adopting 30×30 FE in the mid-surface discretization. Note that, in the case of these proposed through-the-thickness distributions, the nondimensional coordinate $z/h = 0.5$ corresponds to the internal surface of the 3D domain, since the local $\mathbf{g}_3$ direction is considered positive along the inner side of the volume. The displacement distributions proposed in terms of components u_x match the reference solutions in some particular cases, such as 20×20 Q9 + 1LE2 and 20×20 Q16 + 2LE2, where a maximum relative error of 0.088 % is found between the maximum values of the two solutions; minor differences instead are observed when adopting the other proposed discretization models, where again a maximum value of the relative percentage difference (comparable across the remaining models) of 0.39 % is found. In conclusion, all the models proposed have been assessed in terms of displacement predictions, and accurate results have been found across models. Fig. 13 shows the comparison between the displacement magnitude contour obtained using the 20×20 Q9 + 1LE2 CUF model and the 3D ABAQUS model. The global deformed configurations are in a good agreement, and a maximum relative error of 0.9090 % is observed between the maximum displacement magnitudes.

Moreover, the 3D stress analysis of the proposed case is performed to assess the influence of FE mesh and the theory of structure approximation on the stress distributions, again evaluated along the A-B line where the displacement components have already been evaluated. Fig. 14(a), (c) and (e) depict the through-the-thickness distribution of normal stress components computed by higher-order curvilinear 2D CUF models, comparing the results with the 3D ABAQUS solution, when a 20×20 FE is adopted in the discretization of the reference mid-surface. The same comparison is proposed in Fig. 14(b), (d) and (f) considering instead a 30×30 FE discretization. In the proposed results, the quadratic Q9 and the cubic Q16 FE models are adopted to assess the influence of the polynomial order of approximation on the stress components considered. Similar considerations can also be addressed for the results in terms of stress distributions. Consistent solutions in terms of σ_{yy} and σ_{zz} components are obtained in all the cases considered, either in terms of FE discretization or the through-the-thickness expansion models, where major differences are observed in the same case reported for the displacement distributions. Both distributions and nominal values observed are inconsistent with respect to the reference solution, and this can be attributed to the different displacement gradients (namely, then, the strain) directly affecting the stress components. Instead, for the other considered model, the parabolic behavior of normal stress components is consistently obtained, where minor discrepancies are observed again in correspondence with the inner surface where the normal pressure is applied. The maximum relative error of around 23.82 % between stress distributions in correspondence with the inner surface, for $z/h = 0.5$, is observed in the case of 20×20 Q9 + 1LE3 and 20×20 Q9 + 2LE3 models. These discrepancies with respect to the reference solution are attributed to the different behavior of the stress distribution, where a linear behavior is observed in the reference solution given by the parabolic FE model used in the 3D discretization, which is not able to capture local stress variation that the higher-order theory of structures can instead compute. Instead, in the case of the normal σ_{xx} component, major differences are observed when lower-order expansion models are considered. Moreover, the influence of the FE discretization on the results is almost negligible, compared to the strong influence of the through-the-thickness expansion that is influencing the global 3D stress states. Accurate predictions are observed for coarser discretization, but accuracy and convergence are achieved when higher-order models are adopted.

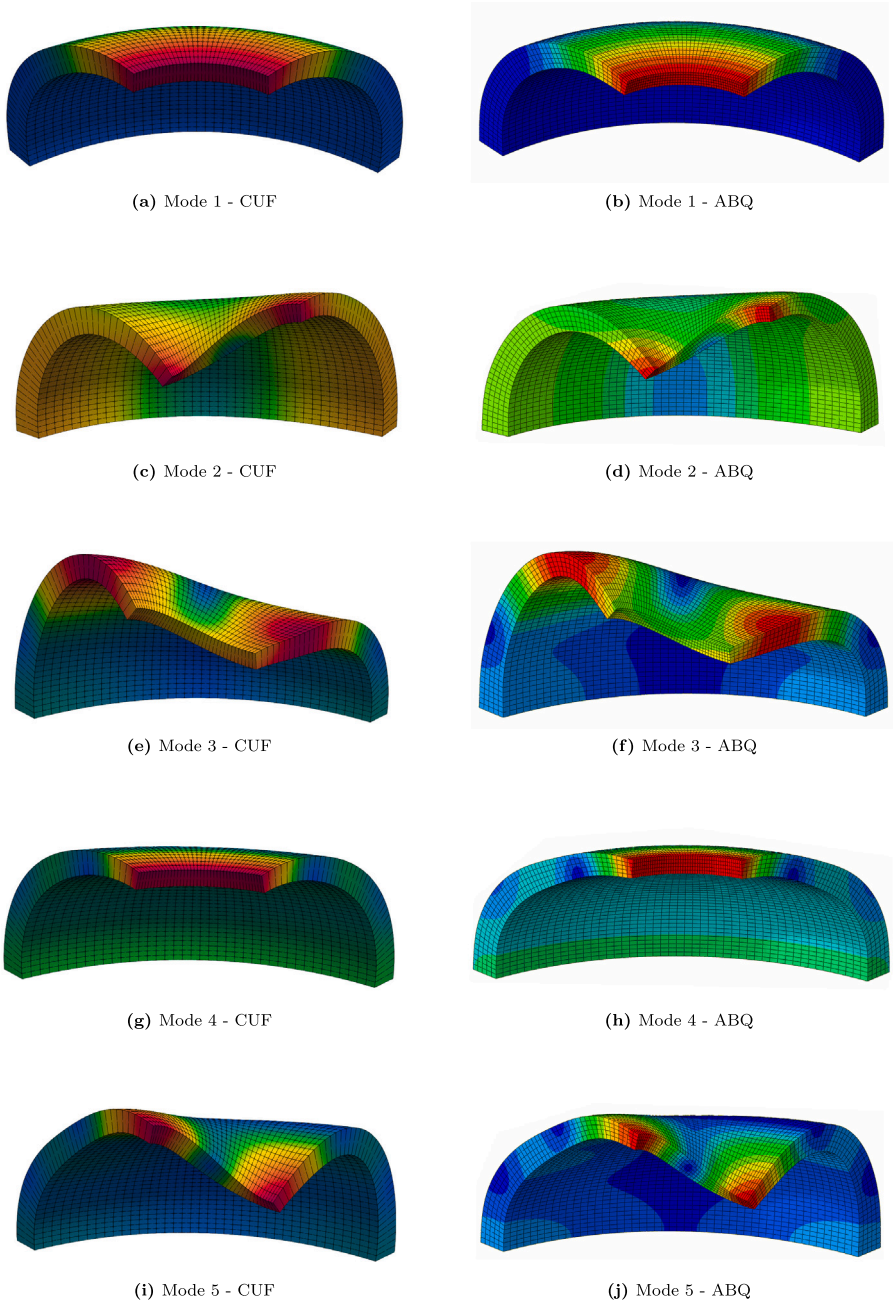

(a) Mode 1 - CUF (b) Mode 1 - ABQ

(c) Mode 2 - CUF (d) Mode 2 - ABQ

(e) Mode 3 - CUF (f) Mode 3 - ABQ

(g) Mode 4 - CUF (h) Mode 4 - ABQ

(i) Mode 5 - CUF (j) Mode 5 - ABQ

Fig. 11. Variable thickness and curvature structures, spherical-like curved structure $R(\Psi) = R_0 \cos^2(\Psi)$: first five normal modes of vibration, graphical representation. Eigenvectors obtained from the 40×40 Q9 + 1LE3 CUF model.

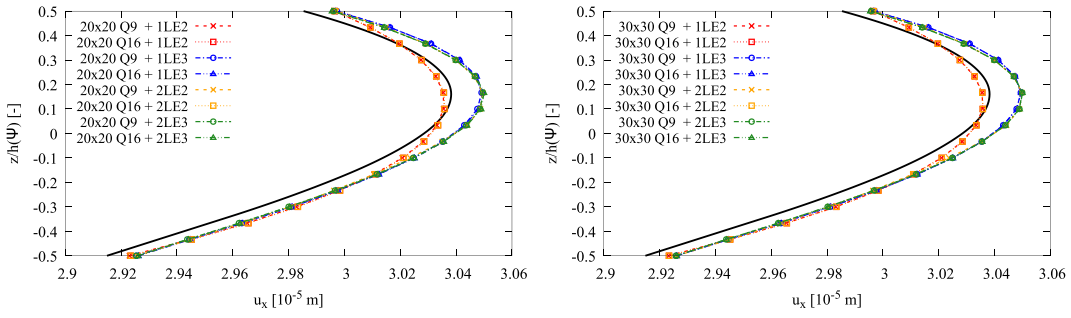

(a) Mesh 20x20 (b) Mesh 30x30

Fig. 12. Variable thickness and curvature structures, catenary structure $R(\Psi) = R_0 \cos^2(\Psi)$: through-the-thickness transversal u_x displacement component distribution, evaluated along the AB line. The reference 3D solution is reported in the black line.

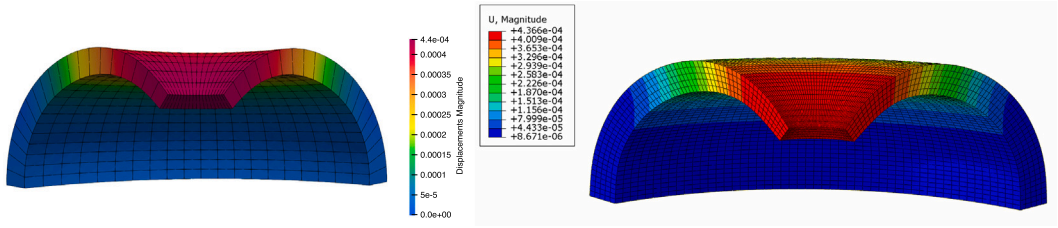

(a) 2D CUF (b) 3D ABQ

Fig. 13. Variable thickness and curvature structures, spherical-like curved structure $R(\Psi) = R_0 \cos^2(\Psi)$: displacement magnitude countour, comparison between 2D CUF solution and 3D ABAQUS reference.

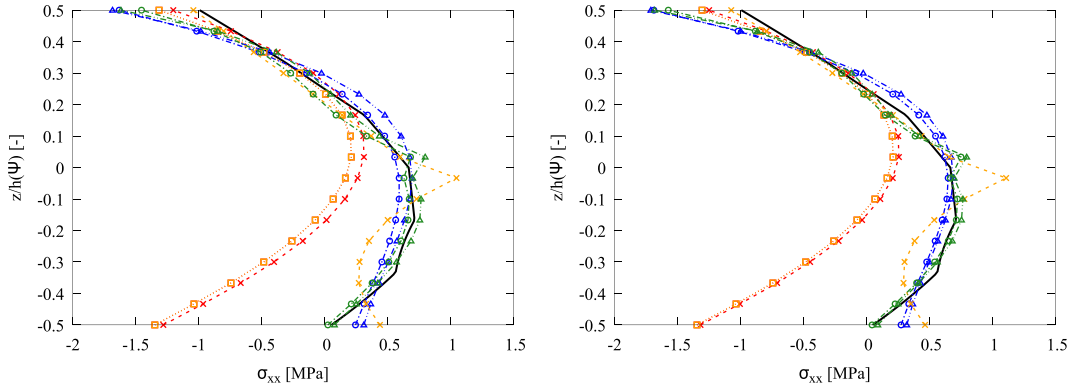

(a) σ_{xx} - 20×20 FE mesh (b) σ_{xx} - 30×30 FE mesh

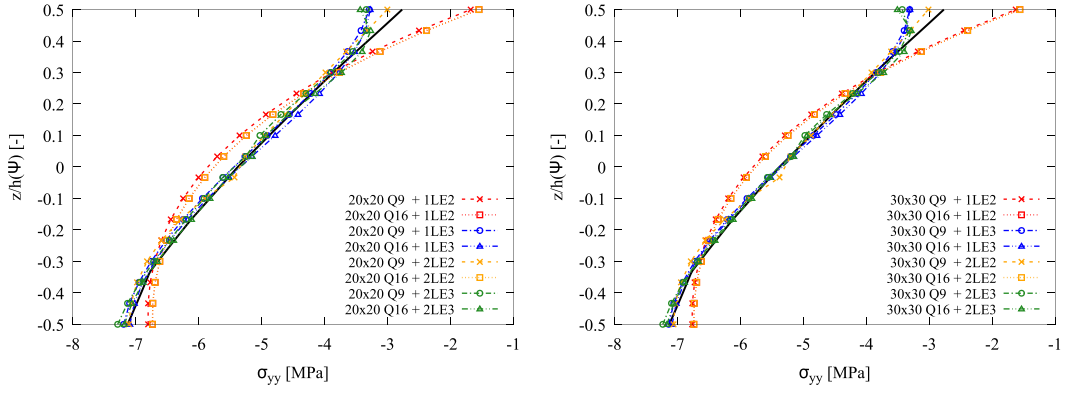

(c) σ_{yy} - 20×20 FE mesh (d) σ_{yy} - 30×30 FE mesh

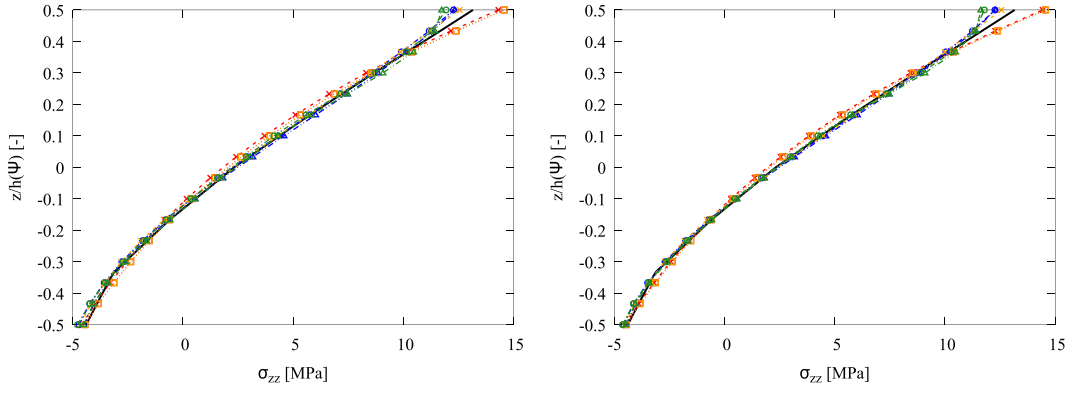

(e) σ_{zz} - 20×20 FE mesh (f) σ_{zz} - 30×30 FE mesh

Fig. 14. Variable thickness and curvature structures, spherical-like curved structure $R(\Psi) = R_0 \cos^2(\Psi)$, stress analysis: through-the-thickness stress component distribution, evaluated at the $y = 0$ section along the AB line. Comparison between higher order 2D CUF models and 3D elasticity ABAQUS solution, obtained with different FE discretization along the mid-surface.

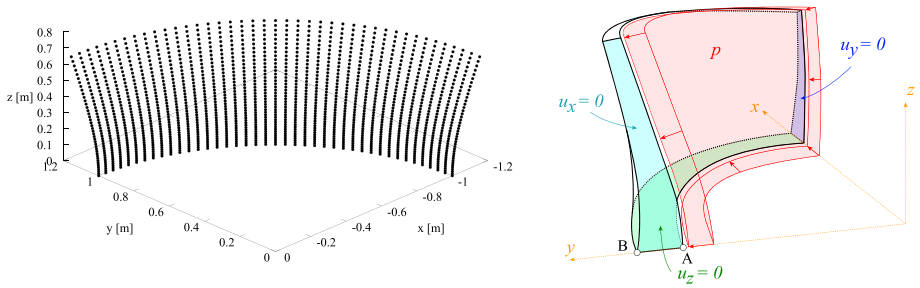

(a) Reference mid-surface discretization (b) Boundary conditions

Fig. 15. Variable thickness and curvature structures, catenary structure $R(\Psi) = R_0 \sec^2(\Psi)$: geometrical features and boundary conditions considered.

Table 4
Catenary structure $R(\Psi) = R_0 \sec^2(\Psi)$, double curvature and double thickness variation case, $\alpha = 3$ case: convergence analysis on natural frequencies [Hz]. Comparison between 2D CUF curvilinear models and 3D elasticity solutions. In brackets, the percentage difference of the proposed solutions.

Mesh	Exp. model	Mode 1	Mode 2	Mode 3	Mode 4	Mode 5	DOF
10 × 10 Q9	1 LE2	66.16(2.82 %)	351.47(1.83 %)	435.06(5.61 %)	512.35(1.43 %)	607.93(−0.45 %)	3969
	1 LE3	66.11(2.75 %)	351.08(1.72 %)	434.54(5.48 %)	511.76(1.32 %)	607.73(−0.49 %)	8649
	2 LE2	66.11(2.75 %)	351.11(1.72 %)	434.57(5.49 %)	511.79(1.32 %)	607.74(−0.48 %)	6615
	2 LE3	66.11(2.75 %)	351.08(1.71 %)	434.53(5.48 %)	511.75(1.32 %)	607.72(−0.49 %)	9261
20 × 20 Q9	1 LE2	65.93(2.47 %)	349.56(1.28 %)	428.56(4.03 %)	505.54(0.09 %)	607.64(0.50 %)	15,129
	1 LE3	65.88(2.40 %)	349.24(1.18 %)	428.12(3.92 %)	505.06(0.01 %)	607.44(0.53 %)	20,172
	2 LE2	65.89(2.40 %)	349.26(1.19 %)	428.15(3.93 %)	505.09(0.00 %)	607.45(0.53 %)	25,215
	2 LE3	65.88(2.40 %)	349.23(1.18 %)	428.12(3.92 %)	505.05(0.01 %)	607.43(0.54 %)	35,301
30 × 30 Q9	1 LE2	65.91(2.45 %)	349.44(1.24 %)	427.91(3.87 %)	504.92(0.04 %)	607.61(0.51 %)	33,489
	1 LE3	65.87(2.38 %)	349.12(1.15 %)	427.51(3.77 %)	504.47(0.12 %)	607.41(0.54 %)	44,652
	2 LE2	65.87(2.38 %)	349.14(1.15 %)	427.53(3.78 %)	504.50(0.12 %)	607.42(0.54 %)	55,815
	2 LE3	65.87(2.37 %)	349.11(1.15 %)	427.50(3.77 %)	504.47(0.13 %)	607.40(0.54 %)	78,141
ABQ	C3D20	64.340	345.159	411.962	505.105	610.700	133,032

6.2.3. Double curvature variation and double thickness variation

Instead, this proposed case study analyzes the catenary-like structure with radius law $R(\Psi) = R_0 \sec^2(\Psi)$. The structure is again made of steel; the material constants considered are Young's modulus $E = 210$ GPa, Poisson's ratio $\nu = 0.33$, and density $\rho = 7850$ kg/m^3. Now, a double variation of the thickness is analyzed, both along the $\mathbf{g}_1$ and $\mathbf{g}_2$ directions. Given the opening angle denoted by $\theta_{op} = 90°$ (due to the symmetry), the local thickness of the structure, defined for each node, is computed by adopting a linear variation law in the $\mathbf{g}_1$ direction:

$$\hat{h}_{\mathbf{g}_1}(\Psi, \theta) = h_{\mathbf{g}_3}(\Psi) + \frac{\theta}{\theta_{op}} \left(\frac{h_{\mathbf{g}_3}(\Psi)}{\alpha} - h_{\mathbf{g}_3}(\Psi) \right) \qquad \theta \in [0, \vartheta_{op} = 90°] \quad (57)$$

where α is a generic scaling factor by which it is possible to define any arbitrary variation in thickness along the tangential $\mathbf{g}_1$ direction. In this way, at $\theta = \theta_{op}$, the local thickness value is set to $h_{\mathbf{g}_3}(\Psi)/\alpha$. Fig. 15(a) shows a representative discretization of the reference mid-surface obtained by the procedure described earlier.

The assessment of the accuracy and efficiency of the present model is carried out by a modal analysis, considering the first five natural frequencies of a curved structure with reference geometrical features listed in Table 2 with $\alpha = 3$. The effects of the mid-surface discretization model and expansion theory adopted on the modal behavior of the structure are again both investigated. In the present analysis, parabolic Q9 (nine-node) FE models are again adopted in the discretization of the reference mid-surface, considering different CUF LE models for the through-the-thickness expansion discretization along the $\mathbf{g}_3$ direction. For convergence reasons, assessed by the previous case study, only the 10×10, 20×20, and 30×30 meshes are analyzed. The numerical results of the present implementation of curvilinear CUF elements are compared against a reference solution computed by a full 3D ABAQUS model. Specifically, the structure is modeled with 15180 C3D20 hexahedral elements.

Table 4 shows the first five natural frequencies of the catenary-like structure with $\alpha = 3$, analyzing again the influence of theory of structure approximation and FE reference mid-surface discretization on the structural modal behavior, comparing extensively the proposed results obtained with curvilinear 2|3D models and reference 3D ABAQUS models. As done in the previous case study, the computational cost is measured in total DOF and the relative percentage difference is reported in brackets. From the proposed analysis, accurate results with relative percentage differences below 5 % are observed in all the mathematical models considered, with perfectly matching solutions in particular mode numbers. Fig. 16 shows the first four normal modes of vibrations, plotting the eigenvectors computed by the numerical simulation adopting the 30×30 Q9 + 2LE2 CUF model and comparing the mode shapes obtained with the one of the reference 3D solution.

In this particular case, these differences have been attributed to the issues related to the 3D modeling with CAD software of such structures, where the 3D geometry is not perfectly generated by exact mathematical expressions but with features that can generate discrepancies in the final 3D model.

Afterwards, the linear static analysis of the same structure is performed, considering symmetric boundary conditions and the application of a constant internal normal pressure, applied in $\mathbf{g}_3$ local direction, with an amplitude of $p = 1$ MPa. Fig. 15(b) depicts the boundary conditions and the load applied. In the following, the influence of the mathematical model adopted in the structure discretization is analyzed by comparing the through-the-thickness distribution of Cartesian displacements and stress components, analyzed at the $y = 0$ symmetry section in correspondence with the $x - y$ symmetry plane, namely along the line given by the A-B point as proposed in the previous case study. Again, also in these proposed through-the-thickness distributions, the nondimensional coordinate $z/h = 0.5$ corresponds to the internal surface of the 3D domain

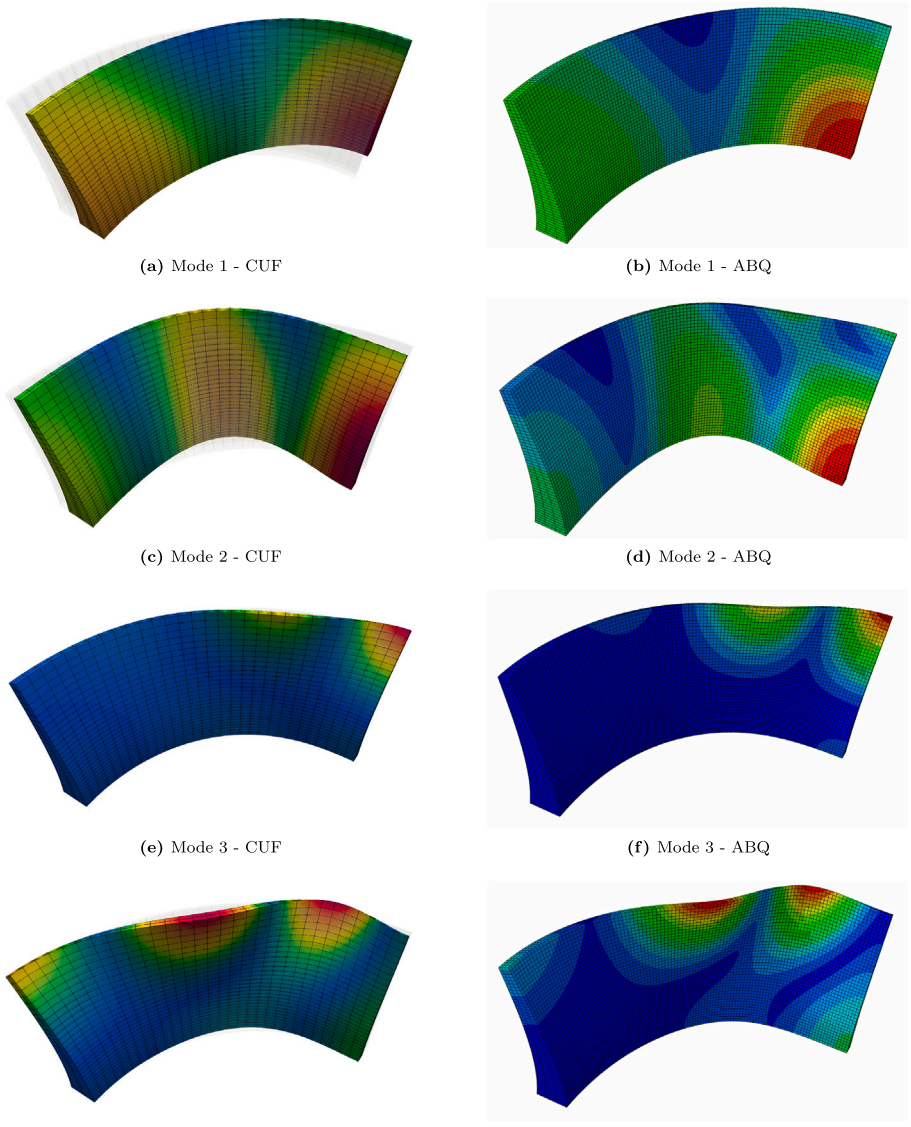

(a) Mode 1 - CUF (b) Mode 1 - ABQ

(c) Mode 2 - CUF (d) Mode 2 - ABQ

(e) Mode 3 - CUF (f) Mode 3 - ABQ

(g) Mode 4 - CUF (h) Mode 4 - ABQ

Fig. 16. Variable thickness and curvature structures, catenary structure $R(\Psi) = R_0 \sec^2(\Psi)$: first four normal modes of vibration, graphical representation. Eigenvectors obtained from the 30×30 Q9 + 2LE2 CUF model.

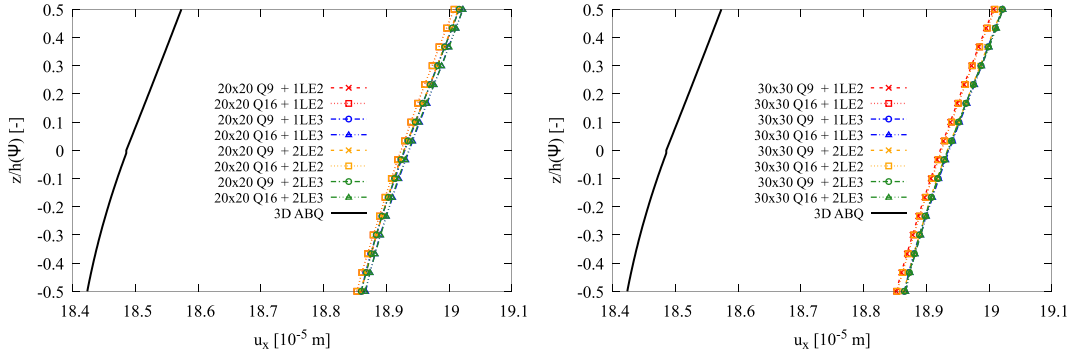

(a) Mesh 20×20 (b) Mesh 30×30

Fig. 17. Variable thickness and curvature structures, catenary structure $R(\Psi) = R_0 \sec^2(\Psi)$: through-the-thickness transversal u_x displacement component distribution, evaluated at the $y = 0$ section along the AB line.

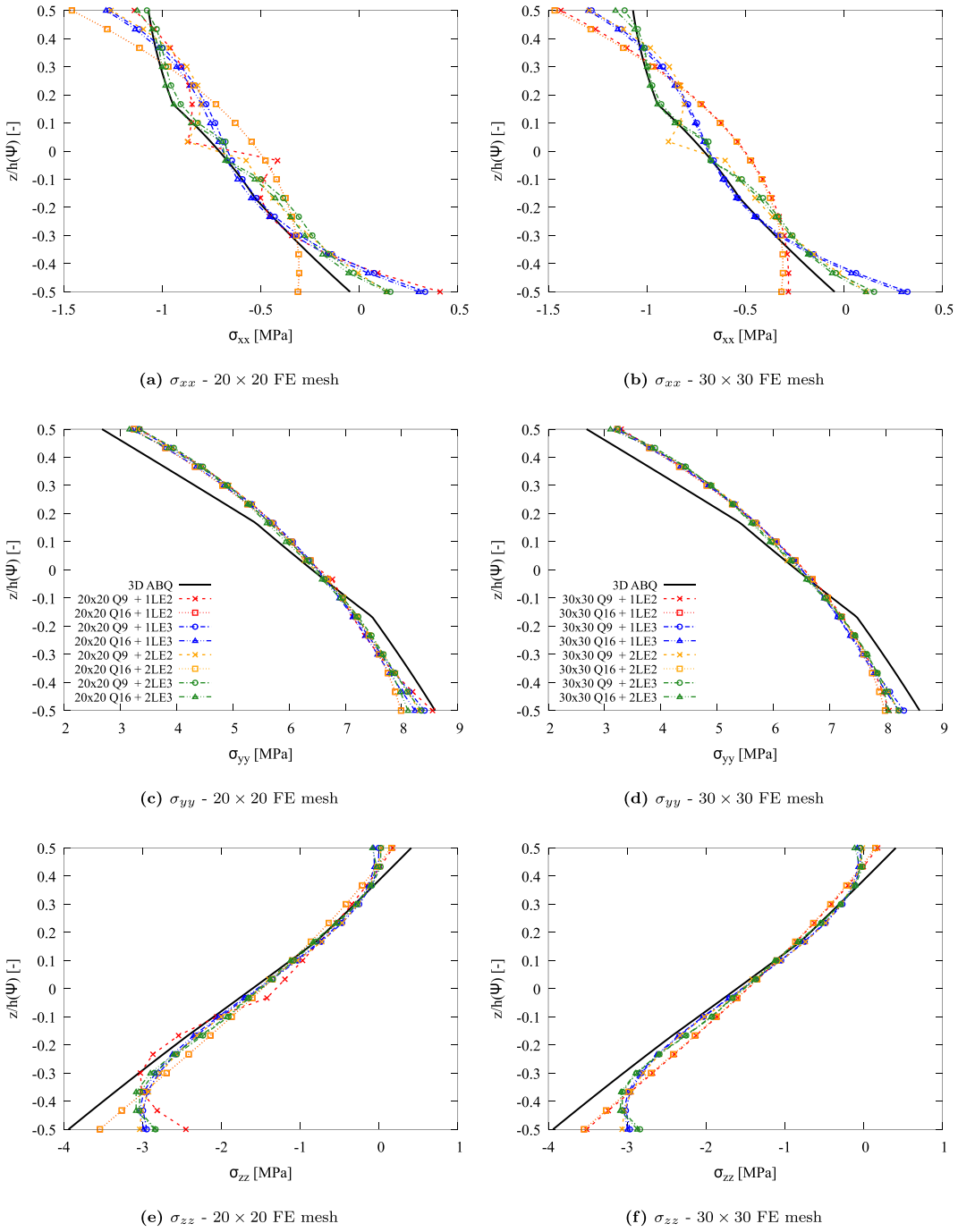

(a) σ_{xx} - 20×20 FE mesh (b) σ_{xx} - 30×30 FE mesh

(c) σ_{yy} - 20×20 FE mesh (d) σ_{yy} - 30×30 FE mesh

(e) σ_{zz} - 20×20 FE mesh (f) σ_{zz} - 30×30 FE mesh

Fig. 18. Variable thickness and curvature structures, catenary structure $R(\Psi) = R_0 \sec^2(\Psi)$, stress analysis: through-the-thickness stress component distribution, evaluated at the $y = 0$ section along the AB line. Comparison between higher-order 2D CUF models obtained with different FE discretization along the mid-surface.

since the local $\mathbf{g}_3$ direction is considered positive along the inner side of the volume.

Fig. 17 shows the through-the-thickness transversal displacement distribution, which is given by the u_x component, for different discretization models along the reference mid-surface and CUF expansion models. Fig. 17(a) shows the displacement distributions when 20×20 FE are adopted in the reference mid-surface discretization, using parabolic Q9 and cubic Q16 2D elements. The same comparison is proposed in Fig. 17(b) adopting 30×30 FE in the mid-surface discretization. In both cases, the results are compared against the reference solution obtained with ABAQUS commercial software and the discretization model listed before in the case of the modal analysis. The results obtained with 2D CUF models are in good agreement with the reference solution, which, however, suffers from high sensibility from the geometric description and model generation due to the impossibility of replicating the exact same geometry with such feature variation. However, small percentage differences are measured, and the maximum relative error measured is 2.35 % in correspondence with the outer surface $z/h = -0.5$. As noted, small differences are observed when refined discretizations are adopted, and consistent results are obtained between different mathematical models adopted in the FE discretization of the structure.

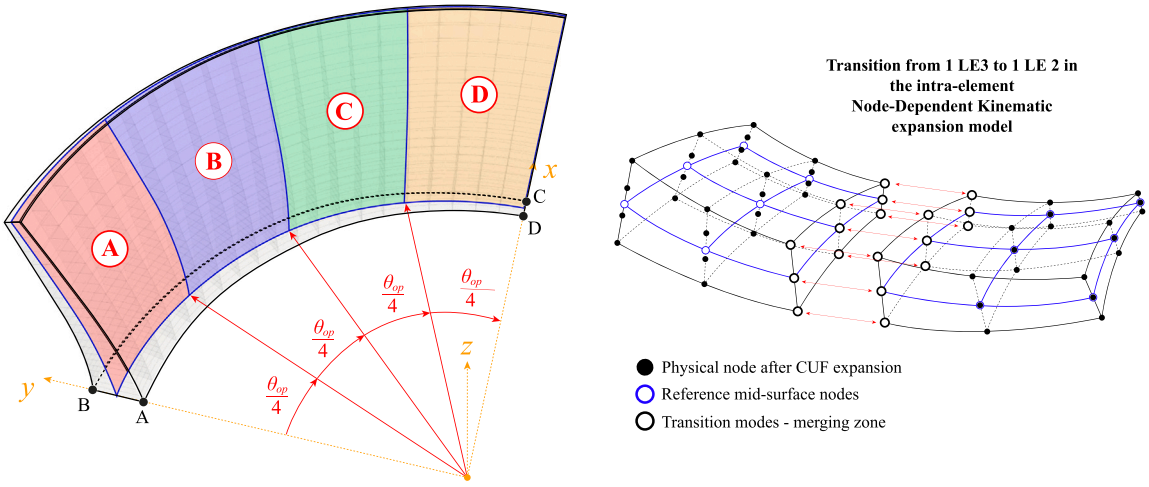

Fig. 19. Variable thickness and curvature structures, catenary structure $R(\Psi) = R_0 \sec^2(\Psi)$: example of transition kinematic model in the mid-surface discretization from LE3 to LE2.

Again, the 3D stress analysis of the proposed case is performed to assess the influence of FE mesh and the theory of structure approximation on the stress distributions. Fig. 18(a), (c), (e) and (g) shows the through-the-thickness distribution of normal and transverse shear stress components computed by higher-order curvilinear 2D CUF models when a 20×20 FE is adopted in the discretization of the reference mid-surface. Again, the stress distributions obtained via 2D CUF models have been compared against reference solution obtained with ABAQUS commercial software. The same comparison is proposed in Fig. 18(b), (d), (f) and (h) considering instead a 30×30 FE discretization. Again, the quadratic Q9 and the cubic Q16 FE models are adopted to assess the influence of the polynomial order of approximation on the stress components considered. Spurious non-consistent solutions are observed when lower orders of approximation are considered in the through-the-thickness expansion regarding the σ_{xx} components; instead, consistent solutions in terms of σ_{yy} and σ_{zz} components are obtained in all the cases considered, either in terms of FE discretization or the through-the-thickness expansion models. Moreover, the influence of the FE discretization on the results is almost negligible; instead, a strong influence of the through-the-thickness expansion on the global 3D stress states is observed, particularly in the transverse component. Accurate predictions are observed for coarser discretization, but accuracy and convergence are achieved when higher-order models are taken into account. The compatibility conditions at the structural edges are observed only when higher-order models are considered, but minor differences are attributed to the numerical issue of approximation in the numerical quadrature of the proposed model since the local co- and contra-variant bases between the Gauss Points and the physical reference surfaces are different. This issue can be partially addressed by adopting refined expansion models.

Afterwards, the NDK approach is exploited in the numerical modeling of variable thickness structures to define different mathematical discretizations within the structural domain. In particular, from the previous analysis, more refined discretizations and higher-order models

Table 5
Variable thickness and curvature structures, catenary structure $R(\Psi) = R_0 \sec^2(\Psi)$, NDK model analysis: comparison of the normal displacement component evaluated at points A and B comparing the accuracy of FE models with transition zones over the reference mid-surface.

Expansion model	20×20 Q9			30×30 Q9		
	u_{x_A} [$\cdot10^{-4}$ m]	u_{x_B} [$\cdot10^{-4}$ m]	DOF	u_{x_A} [$\cdot10^{-4}$ m]	u_{x_B} [$\cdot10^{-4}$ m]	DOF
1LE3-1LE2-1LE2-1LE2	$1.9009^{(0.03\ \%)}$	$1.8854^{(0.03\ \%)}$	16,359	$1.9014^{(0.03\ \%)}$	$1.8859^{(0.03\ \%)}$	36,234
1LE3-1LE3-1LE2-1LE2	$1.9014^{(0.01\ \%)}$	$1.8858^{(0.01\ \%)}$	17,589	$1.9018^{(0.01\ \%)}$	$1.8863^{(0.01\ \%)}$	38,796
1LE3-1LE3-1LE3-1LE2	$1.9015^{(0.00\ \%)}$	$1.8860^{(0.00\ \%)}$	18,696	$1.9020^{(0.00\ \%)}$	$1.8865^{(0.00\ \%)}$	41,358
Uniform 1LE3	1.9016	1.8860	20,172	1.9021	1.8865	44,652
2LE3-2LE2-2LE2-2LE2	$1.9015^{(0.00\ \%)}$	$1.8859^{(0.00\ \%)}$	27,675	$1.9020^{(0.00\ \%)}$	$1.8865^{(0.00\ \%)}$	61,305
2LE3-2LE3-2LE2-2LE2	$1.9015^{(0.00\ \%)}$	$1.8860^{(0.00\ \%)}$	30,135	$1.9020^{(0.00\ \%)}$	$1.8865^{(0.00\ \%)}$	66,429
2LE3-2LE3-2LE3-2LE2	$1.9016^{(0.00\ \%)}$	$1.8860^{(0.00\ \%)}$	32,349	$1.9021^{(0.00\ \%)}$	$1.8865^{(0.00\ \%)}$	71,553
Uniform 2LE3	1.9016	1.8860	35,301	1.9021	1.8865	78,141
Expansion model	20×20 Q16			30×30 Q16		
	u_{x_A} [$\cdot10^{-4}$ m]	u_{x_B} [$\cdot10^{-4}$ m]	DOF	u_{x_A} [$\cdot10^{-4}$ m]	u_{x_B} [$\cdot10^{-4}$ m]	DOF
1LE3-1LE2-1LE2-1LE2	$1.9016^{(0.03\ \%)}$	$1.8860^{(0.03\ \%)}$	36,234	$1.9016^{(0.03\ \%)}$	$1.8860^{(0.03\ \%)}$	80,535
1LE3-1LE3-1LE2-1LE2	$1.9020^{(0.01\ \%)}$	$1.8864^{(0.01\ \%)}$	38,796	$1.9020^{(0.01\ \%)}$	$1.8865^{(0.01\ \%)}$	86,268
1LE3-1LE3-1LE3-1LE2	$1.9022^{(0.00\ \%)}$	$1.8866^{(0.00\ \%)}$	41,358	$1.9022^{(0.00\ \%)}$	$1.8867^{(0.00\ \%)}$	92,274
Uniform 1LE3	1.9022	1.8867	44,652	1.9022	1.8867	99,372
2LE3-2LE2-2LE2-2LE2	$1.9021^{(0.00\ \%)}$	$1.8866^{(0.00\ \%)}$	61,305	$1.9022^{(0.00\ \%)}$	$1.8866^{(0.00\ \%)}$	136,227
2LE3-2LE3-2LE2-2LE2	$1.9022^{(0.00\ \%)}$	$1.8866^{(0.00\ \%)}$	66,429	$1.9022^{(0.00\ \%)}$	$1.8866^{(0.82\ \%)}$	147,693
2LE3-2LE3-2LE3-2LE2	$1.9022^{(0.00\ \%)}$	$1.8866^{(0.00\ \%)}$	71,553	$1.9022^{(0.00\ \%)}$	$1.8867^{(0.82\ \%)}$	159,705
Uniform 2LE3	1.9022	1.8866	78,141	1.9022	1.8867	173,901

Table 6
Variable thickness and curvature structures, catenary structure $R(\Psi) = R_0 \sec^2(\Psi)$, NDK model analysis: comparison of the normal displacement component evaluated at points C and D comparing the accuracy of FE models with transition zones over the reference mid-surface.

Expansion model	20×20 Q9			30×30 Q9		
	u_{y_C} [$\cdot 10^{-4}$ m]	u_{y_D} [$\cdot 10^{-4}$ m]	DOF	u_{y_C} [$\cdot 10^{-4}$ m]	u_{y_D} [$\cdot 10^{-4}$ m]	DOF
1LE3-1LE2-1LE2-1LE2	$-1.1433^{(0.06\ \%)}$	$-1.1597^{(0.06\ \%)}$	16,359	$-1.1446^{(0.06\ \%)}$	$-1.1610^{(0.06\ \%)}$	36,234
1LE3-1LE3-1LE2-1LE2	$-1.1438^{(0.02\ \%)}$	$-1.1602^{(0.02\ \%)}$	17,589	$-1.1450^{(0.02\ \%)}$	$-1.1615^{(0.02\ \%)}$	38,796
1LE3-1LE3-1LE3-1LE2	$-1.1439^{(0.01\ \%)}$	$-1.1604^{(0.01\ \%)}$	18,696	$-1.1452^{(0.01\ \%)}$	$-1.1617^{(0.01\ \%)}$	41,358
Uniform 1LE3	-1.1440	-1.1605	20,172	-1.1453	-1.1617	44,652
2LE3-2LE2-2LE2-2LE2	$-1.1439^{(0.00\ \%)}$	$-1.1603^{(0.00\ \%)}$	27,675	$-1.1452^{(0.00\ \%)}$	$-1.1616^{(0.00\ \%)}$	61,305
2LE3-2LE3-2LE2-2LE2	$-1.1440^{(0.00\ \%)}$	$-1.1604^{(0.00\ \%)}$	30,135	$-1.1452^{(0.00\ \%)}$	$-1.1616^{(0.00\ \%)}$	66,429
2LE3-2LE3-2LE3-2LE2	$-1.1440^{(0.00\ \%)}$	$-1.1604^{(0.00\ \%)}$	32,349	$-1.1452^{(0.00\ \%)}$	$-1.1616^{(0.00\ \%)}$	71,553
Uniform 2LE3	-1.1440	-1.1604	35,301	-1.1452	-1.1617	78,141
Expansion model	20×20 Q16			30×30 Q16		
	u_{y_C} [$\cdot 10^{-4}$ m]	u_{y_D} [$\cdot 10^{-4}$ m]	DOF	u_{y_C} [$\cdot 10^{-4}$ m]	u_{y_D} [$\cdot 10^{-4}$ m]	DOF
1LE3-1LE2-1LE2-1LE2	$-1.1450^{(0.06\ \%)}$	$-1.1614^{(0.06\ \%)}$	36,234	$-1.1450^{(0.06\ \%)}$	$-1.1614^{(0.06\ \%)}$	80,535
1LE3-1LE3-1LE2-1LE2	$-1.1454^{(0.02\ \%)}$	$-1.1618^{(0.02\ \%)}$	38,796	$-1.1455^{(0.02\ \%)}$	$-1.1619^{(0.02\ \%)}$	86,268
1LE3-1LE3-1LE3-1LE2	$-1.1456^{(0.00\ \%)}$	$-1.1620^{(0.00\ \%)}$	41,358	$-1.1457^{(0.00\ \%)}$	$-1.1621^{(0.00\ \%)}$	92,274
Uniform 1LE3	-1.1456	-1.1621	44,652	-1.1457	-1.1621	99,372
2LE3-2LE2-2LE2-2LE2	$-1.1456^{(0.00\ \%)}$	$-1.1620^{(0.00\ \%)}$	61,305	$-1.1457^{(0.00\ \%)}$	$-1.1620^{(0.00\ \%)}$	136,227
2LE3-2LE3-2LE2-2LE2	$-1.1456^{(0.00\ \%)}$	$-1.1620^{(0.00\ \%)}$	66,429	$-1.1457^{(0.00\ \%)}$	$-1.1620^{(0.00\ \%)}$	147,693
2LE3-2LE3-2LE3-2LE2	$-1.1456^{(0.00\ \%)}$	$-1.1620^{(0.00\ \%)}$	71,553	$-1.1457^{(0.00\ \%)}$	$-1.1621^{(0.00\ \%)}$	159,705
Uniform 2LE3	-1.1456	-1.1620	78,141	-1.1457	-1.1621	173,901

are required when thick structures are considered; instead, lower-order models can be adopted in thin structures. From this last consideration, the catenary structure here is remodeled, adopting higher-order models where higher thickness is considered and lower-order models in the thinner corners of the same structure. To achieve this, the reference mid-surface of the catenary structure is divided into four different zones (A-D), where different expansion models will be considered, to define globally computationally efficient and accurate models by considering higher-order models only where needed. A graphical representation of the following approach is provided in Fig. 19. The coupling between different theories of structural approximation in transition zones is straightforwardly obtained by considering different intra-element CUF expansions through the NDK approach. In this way, one can define geometrically consistent models and naturally achieve the merging between different models and finite elements, following the FEM-CUF assembling procedure described in [59,60]. The results are expressed regarding mechanical response measured in the physical points A-D, reported in the same figure.

Again, the same static analysis performed before is now considered adopting NDK models instead of uniform expansion models. The influence of the different through-the-thickness expansion models and the effect of different zones on the global mechanical behavior of the structures are investigated considering six different models are here considered by employing parabolic and cubic expansion models in the thinner and thicker structural corners, respectively. In particular, higher-order models will always be considered in the thick corner of the structure (zone A), and less refined models will be adopted in the remaining zones. In the following, the adopted models will be indicated as Mod.A-Mod.B-Mod.C-Mod.D, explicitly indicating the theory of structure approximation adopted in the specific zone, following the nomenclature defined in Fig. 19. Table 5 shows the transversal displacement components computed at points A-B, comparing the results obtained by adopting NDK transition models and uniform discretization models, and computing the relative percentage difference with respect to the respective uniform model (reported in brackets). A similar comparison is proposed for points C-D in Table 6. In the proposed analysis, the effects of the FE discretization along the reference mid-surface, the polynomial order of FE mesh, and the theory of structure approximation are analyzed, considering different transition models. For each model considered, the total computational cost required by the simulation is measured in terms of total DOF. The results show a perfect match across the solutions obtained from different models. In particular, accurate results are obtained with less refined models with respect to the uniform mesh models, demonstrating the capabilities of the present model to further reduce computational costs by employing transitional meshes, built ad-hoc based on the individual geometric properties of the structure, overcoming the aspect-ratio limitations imposed by the use of refined 3D model at thick corners of the structure, which would impose a large number of highly deformed finite elements in the thin corners. Furthermore, it is possible to observe that the same solutions in terms of displacements can be obtained by adopting lower-order models in the reference mid-surface discretization, without the need for computationally expensive models based on cubic 2D interpolation, demonstrating the efficiency of the present approach. Additionally, the adoption of NDK models, which allow the definition of FE with different through-the-thickness kinematics for each node, allows the definition of transitional meshes by avoiding special coupling techniques between elements, taking advantage only of the CUF assembly technique and the superimposition of finite nodes in connection zones [50,59].

7. Conclusions

This paper presents a novel curvilinear finite element (FE) formulation for the static and modal analysis of shells with arbitrary curvature and variable thickness. The presented 3D-like elements are isoparametric and formulated in the framework of Carrera Unified Formulation (CUF) by using Lagrange approximating functions along the thickness and fully curvilinear coordinates in the three-spatial directions, resulting in a pure displacement-based FE model in which different orders of approximation are embedded employing the Node-Dependent Kinematics (NDK) approach naturally. Since the transformation from Cartesian coordinates to curvilinear local coordinates is performed through a 3D Jacobian matrix, the resulting elements, differently from classical shell ones, are able to model non-orthogonal geometries and geometrical features variation within the element domain. Although these elements behave as 3D ones from a geometrical point of view, allowing to consider the variation of different geometrical features, such as curvature or thickness, their computational cost is comparable to classical CUF shell elements because a different order of approximation can be adopted along the thickness with respect to the approximation used on the mid-surface.

The capabilities of the present curvilinear models are investigated by performing the static and modal analysis of three shell-like structures: shell with single curvature and single variation of thickness; shell with double curvatures and single variation of thickness; shell with double curvature and double variation of thickness. In the proposed work, only linear variation laws have been adopted for thickness variations along different directions, although it is possible to implement any generic geometry since the 3D reconstruction is performed through the isoparametric approach.

The results are provided in terms of natural frequencies, displacements, strains, and stresses, and they are validated against 3D analyses performed with commercial software employing classical 3D finite elements, which provide the direct explicit solution of the equilibrium equations. The results suggest that:

- The present model is able to handle complex geometrical features and their variation within the element domain without affecting the accuracy of the results;
- A significant reduction in terms of degrees of freedom (DOF) required by the simulation is observed, demonstrating the consistency of the present model to handle complex mechanical behavior relying on higher-order theory of structure approximation;
- The present curvilinear FE model is not affected by the same aspect-ratio constraint of classical hexahedral 3D models since different orders of approximation are adopted within the FE definition, adopting higher-order expansion theories in the thickness direction where needed;
- The hierarchical nature of the elementary blocks of the present models allows to define generic curvilinear FE models independently of the mathematical model adopted in the FE definition. Once the reference mid-surface discretization and through-the-thickness kinematics are assigned, the Fundamental Nuclei (FN) provide directly the elementary blocks of the FE matrices, computed in local curvilinear coordinates and recovered in Cartesian coordinates straightforwardly;
- Since 1D Lagrange polynomials are adopted in the through-the-thickness kinematics, the final model refers only to physical nodes that allow the imposition of generic boundary conditions directly on displacement and load components, differently with respect to classical shell models where rotational degrees of freedom or higher-order derivatives have to be treated;

Future works will extend the present approach to the Unified formulation of curvilinear beam models, the extension of the present model to laminated multilayered structures, and the inclusion of direction-dependent material properties. Furthermore, the extension of the present model to the geometrically nonlinear analysis of structures is intended. In particular, theoretically no limits on the thickness or curvature variations are given by the present approach. An extensive stability analysis and locking investigation are also intended where complex case studies are analyzed with the present 2|3D approach.

CRediT authorship contribution statement

Piero Chiaia: Writing – original draft, Software, Methodology, Investigation, Formal analysis. **Maria Cinefra:** Writing – review & editing, Writing – original draft, Software, Resources, Methodology, Formal analysis, Conceptualization. **Erasmo Carrera:** Supervision, Methodology, Conceptualization.

Declaration of competing interest

The authors declare that they have no known competing financial interests or personal relationships that could have appeared to influence the work reported in this paper.

Appendix A. Explicit expression of the algebraic matrix $\mathbf{B}^{\tau i}_{curv}$

In the present appendix, the explicit expression of the algebraic matrix $\mathbf{B}^{\tau i}_{curv}$ of derivative operators applied to the 3D-like shape functions, written in terms of final Cartesian components $\hat{\mathbf{u}}_{\tau i}$, is provided:

$$\mathbf{B}^{\tau i}_{curv}[1,j] = \frac{\partial L_{\tau i}}{\partial \xi}(\mathbf{g}_1)_j + L_{\tau i}\frac{\partial (\mathbf{g}_1)_j}{\partial \xi} - \Gamma^k_{11} L_{\tau i}(\mathbf{g}_k)_j \tag{58}$$

$$\mathbf{B}^{\tau i}_{curv}[2,j] = \frac{\partial L_{\tau i}}{\partial \eta}(\mathbf{g}_2)_j + L_{\tau i}\frac{\partial (\mathbf{g}_2)_j}{\partial \eta} - \Gamma^k_{22} L_{\tau i}(\mathbf{g}_k)_j \tag{59}$$

$$\mathbf{B}^{\tau i}_{curv}[3,j] = \frac{\partial L_{\tau i}}{\partial \nu}(\mathbf{g}_3)_j + L_{\tau i}\frac{\partial (\mathbf{g}_3)_j}{\partial \nu} - \Gamma^k_{33} L_{\tau i}(\mathbf{g}_k)_j \tag{60}$$

$$\mathbf{B}^{\tau i}_{curv}[4,j] = \frac{\partial L_{\tau i}}{\partial \xi}(\mathbf{g}_3)_j + \frac{\partial L_{\tau i}}{\partial \nu}(\mathbf{g}_1)_j + L_{\tau i}\left[\frac{\partial (\mathbf{g}_3)_j}{\partial \xi} + \frac{\partial (\mathbf{g}_1)_j}{\partial \nu}\right] - 2\Gamma^k_{13} L_{\tau i}(\mathbf{g}_k)_j \tag{61}$$

$$\mathbf{B}^{\tau i}_{curv}[5,j] = \frac{\partial L_{\tau i}}{\partial \eta}(\mathbf{g}_3)_j + \frac{\partial L_{\tau i}}{\partial \nu}(\mathbf{g}_2)_j + L_{\tau i}\left[\frac{\partial (\mathbf{g}_3)_j}{\partial \eta} + \frac{\partial (\mathbf{g}_2)_j}{\partial \nu}\right] - 2\Gamma^k_{23} L_{\tau i}(\mathbf{g}_k)_j \tag{62}$$

$$\mathbf{B}^{\tau i}_{curv}[6,j] = \frac{\partial L_{\tau i}}{\partial \xi}(\mathbf{g}_2)_j + \frac{\partial L_{\tau i}}{\partial \eta}(\mathbf{g}_1)_j + L_{\tau i}\left[\frac{\partial (\mathbf{g}_2)_j}{\partial \xi} + \frac{\partial (\mathbf{g}_1)_j}{\partial \eta}\right] - 2\Gamma^k_{12} L_{\tau i}(\mathbf{g}_k)_j \tag{63}$$

where the symbol $(\cdot)_j$ is used to denote the j-th component of the vector, and repeated index k indicates summation. In the proposed derivation of the algebraic matrix of the strain component, again, one can note the presence of non-null components $(\mathbf{g}_1)_3$, $(\mathbf{g}_2)_3$, $(\mathbf{g}_3)_1$ and $(\mathbf{g}_3)_2$ given by the embedding of possible variation of thickness inside the proposed shell element, as described in Section 4.2.

Appendix B. Numerical integration

Following the definitions of the stiffness and mass matrix FN, given in Eqs. (49) and (50), the 3D volume integral is computed using a numerical quadrature procedure based on Gauss integration. In the proposed approach, the final unknowns of the problem are represented by the standard Cartesian displacement components as provided in Eq. (52), obtained through the application of the transformation law between reference frames. In the following, the 3D integration of stiffness and mass matrix FN is provided:

$$\mathbf{K}^{\tau sij} = \int_\Omega \mathbf{B}^{sj\,T}_{curv}\mathbf{J}^T_{c2c}\mathbb{C}\mathbf{J}_{c2c}\mathbf{B}^{\tau i}_{curv}|\mathbf{J}|\,dV \tag{64}$$

$$\mathbf{M}^{\tau sij} = \rho\int_\Omega L_{sj}(\xi,\eta,\nu)\,\mathbf{I}\,L_{\tau i}(\xi,\eta,\nu)|\mathbf{J}|\,dV \tag{65}$$

The key feature of the present approach is to include the effects of curvature variation and thickness variation in the 3D-like polynomial expansion of the displacement field by means of the numerical approximation of the standard local covariant basis. In the proposed approach, only Lagrange polynomials are adopted in the through-the-thickness approximation of the displacement field, thus the expansion basis $F_\tau(\alpha^3)$ considered will be only composed by 1D Lagrange polynomials and then the final unknowns of the model are the physical Cartesian components of the FE physical nodes. In this way, the 3D-like expansion is given by the physical coordinates of the discretization adopted, in which is straighforwordly included the geometrical feature variation, as introduced in Section 4.1. The proposed approach leverages on the NDK approach by means of the recursive index notation adopted for the displacement field, by which it is possible to adopt different expansion models for each node of the FE model considered along the reference mid-surface.

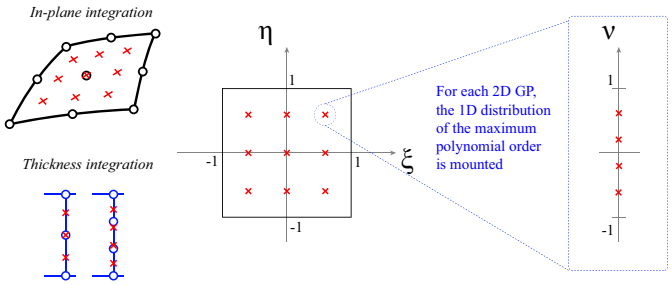

Fig. 20. Numerical integration: 3D distribution of Gauss Point within the 3D curved domain.

Algorithm 1 Elemental numerical integration.

```
Initialize variables
for k = 1 to N_GP do
    Locate the Gauss point (ξ_k, η_k, ν_k)
    for i, j = 1 to N_n (number of finite nodes) do
        for τ, s = 1 to M (number of expansion terms) do
            Compute L_τi and L_sj, and their derivatives with respect to (α^1, α^2, α^3)
            Compute the covariant basis g_i using Eq. (29) and its derivatives with respect to (α^1, α^2, α^3)
        end for
        Sum over τ–s
    end for
    Sum over i–j
    Compute the metric tensor g^ij, the contravariant basis g^i and the Christoffel symbols Γ^i_jk
    for i, j = 1 to N_n (number of finite nodes) do
        for τ, s = 1 to M (number of expansion terms) do
            Compute the algebraic matrices of the strain in curvilinear coordinates, Eqs. (58)–(63), B^sj_curv and B^τi_curv
        end for
    end for
    Compute the transformation matrix J_c2c, Eq. (44)
    Compute the final 3×3 FN matrix
end for
```

In the proposed numerical computation of the FN, by considering the 3D distribution of Gauss Points (GP) in the closed curved domain, the computation of the fundamental matrices required is strictly dependent on the local covariant basis, and the matrix $\mathbf{J}_{c2c}$. These required mathematical quantities are computed by means of the 3D-like shape function inside the loops on the discretization indices, obtaining then the numerical approximation of the local reference frame within the element domain and incorporating in a unified and recursive manner also the geometrical feature variations in the numerical evaluations of integral.

The distribution of Gauss Point within the natural 3D domain used for the computation of integrals is given by the combination of the minimum number of Gauss Point required by each polynomial expansion basis. Starting from the quadrature rule based on the polynomial order of approximation of the 2D reference surface, thus the order of 2D $N_i(\alpha^1, \alpha^2)$, $N_j(\alpha^1, \alpha^2)$ shape function, the GP for the in-plane integration is established. Depending on the node-dependent polynomial order of approximation in the thickness direction, the maximum order of approximation of each set of $F_\tau(\alpha^3)$, $F_s(\alpha^3)$ functions is taken into account. Therefore, the 1D GP distribution for the thickness integration is then established considering the theoretical minimum number required for that maximum order 1D through-the-thickness approximation. Fixing the maximum approximation order and the 1D GP distribution, the quadrature rule is then considered constant for the whole model, even if lower-order approximations are considered in some nodes of the 2D element. The final, 3D, GP adopted for the integration of FE matrices and Fundamental Nuclei is the 3D combination of these two sets. For each 2D $N_i(\alpha^1, \alpha^2)$, $N_j(\alpha^1, \alpha^2)$ GP, the set of 1D GP for the $F_\tau(\alpha^3)$, $F_s(\alpha^3)$ integration is mounted. With this straightforward approach, the theoretical consistency for the Gauss quadrature is naturally achieved and the 3D integration is then performed considering this 3D set of GP. The graphical representation of the GP 3D construction is provided in Fig. 20.

Data availability

Data will be made available upon request.

References

[1] Reddy JN. Finite element and finite volume Methods for heat transfer and fluid dynamics. Cambridge University Press; 2022.
[2] Pagani A, Racionero Sánchez-Majano A, Zamani D, Petrolo M, Carrera E. Fundamental frequency layer-wise optimization of tow-steered composites considering gaps and overlaps. Aerotecn Missili Spazio 2025;104:135–51. https://doi.org/10.1007/s42496-024-00212-w
[3] Silva G, Do Prado A. P, Cabral P. H, De Breuker R, Dillinger J. Tailoring of a composite regional jet wing using the slice and swap method. J Aircr 2019 March;56(3):990–1004. https://doi.org/10.2514/1.C035094
[4] Borwankar P, Zhao W, Kapania R. K, Bansal M. Two-level weight optimization of composite laminates using integer programming. AIAA J 2022;60(11):6436–46. https://doi.org/10.2514/1.J061560
[5] Wang J, Li X, Sun Z, Yang J, Zhang W. Connection between geometric dimension and dynamic response of bistable composite laminate with variable curvatures. Mech Adv Mater Struct 2025 January;1–19. https://doi.org/10.1080/15376494.2025.2451770
[6] Liu T, Wang X. Inverse design of three-dimensional variable curvature pneumatic soft actuators. J Mech Robot 2025 February;17(7). https://doi.org/10.1115/1.4067722
[7] Zhang F, Kim M-Y. A simple but accurate FEM for lateral-torsional buckling loads of mono-symmetric thin-walled beams considering pre-buckling effects. Thin-Walled Struct 2025;206:112676. https://doi.org/10.1016/j.tws.2024.112676
[8] Addessi D, Di Re P, Cimarello G. Enriched beam finite element models with torsion and shear warping for the analysis of thin-walled structures. Thin-Walled Struct 2021;159:107259. https://doi.org/10.1016/j.tws.2020.107259
[9] Güven U. Elastic-plastic annular disk with variable thickness subjected to external pressure. Acta Mech 1992 March;92(1–4):29–34. https://doi.org/10.1007/BF01174165
[10] Syaiful Redzwan MS, Noor Badariah A, Jacob V, Javad E, Mauricio D. P, Viktor M, et al. Analysis of thickness variation in biological tissues using microwave sensors for health monitoring applications. IEEE Access 2019;7:156033–43. https://doi.org/10.1109/ACCESS.2019.2949179
[11] Wang C. M, Reddy J. N. Shear deformable beams and plates. Elsevier Science; 2000.
[12] Reddy J. N. A simple higher-order theory for laminated composite plates. J Appl Mech 1984 December;51(4):745–52.
[13] Reddy J. N, Liu C. F. A higher-order shear deformation theory of laminated elastic shells. Int J Eng Sci 1985;23(3):319–30. https://doi.org/10.1016/0020-7225(85)90051-5
[14] Patni M, Minera S, Weaver P. M, Pirrera A. Efficient modelling of beam-like structures with general non-prismatic, curved geometry. Comput Struct 2020;240:106339. https://doi.org/10.1016/j.compstruc.2020.106339
[15] Ai Q, Weaver P. M. Simplified analytical model for tapered sandwich beams using variable stiffness materials. J Sandwich Struct Mater 2016 August;19(1):3–25. https://doi.org/10.1177/1099636215619775
[16] Sze K. Y. Three-dimensional continuum finite element models for plate/shell analysis. Prog Struct Eng Mater 2002 September;4(4):400–7. https://doi.org/10.1002/pse.133
[17] Aguirre A, Codina R, Baiges J. Stress–displacement stabilized finite element analysis of thin structures using solid-shell elements, Part I: on the need of interpolating the stresses. Finite Elem Anal Des 2024 September;236:104168. https://doi.org/10.1016/j.finel.2024.104168
[18] Yasin M. Y, Khalid H. M, Beg MS. Exact solution considering layerwise mechanics for laminated composite and sandwich curved beams of deep curvatures. Compos Struct 2020 July;244:112258. https://doi.org/10.1016/j.compstruct.2020.112258
[19] Lin K. C, Hsieh C. M. The closed form general solutions of 2-D curved laminated beams of variable curvatures. Compos Struct 2007 August;79(4):606–18. https://doi.org/10.1016/j.compstruct.2006.02.027
[20] Lee B. K, Oh S. J, Mo J. M, Lee T. E. Out-of-plane free vibrations of curved beams with variable curvature. J Sound Vib 2008 November;318(1–2):227–46. https://doi.org/10.1016/j.jsv.2008.04.015
[21] De Pietro G, de Miguel A. G, Carrera E, Giunta G, Belouettar S, Pagani A. Strong and weak form solutions of curved beams via Carrera's unified formulation. Mech Adv Mater Struct 2018 November;27(15):1342–53. https://doi.org/10.1080/15376494.2018.1510066
[22] Liew K. M, Lim C. W. Vibratory characteristics of cantilevered rectangular shallow shells of variable thickness. AIAA J 1994 February;32(2):387–96. https://doi.org/10.2514/3.59996
[23] Kulikov G. M. Three-dimensional elasticity solutions for doubly-curved composite shells by extended differential quadrature method. Compos Struct 2025 January;352:118647. https://doi.org/10.1016/j.compstruct.2024.118647

[24] Jin G, Ye T, Ma X, Chen Y, Su Z, Xie X. A unified approach for the vibration analysis of moderately thick composite laminated cylindrical shells with arbitrary boundary conditions. Int J Mech Sci 2013 October;75:357–76. https://doi.org/10.1016/j.ijmecsci.2013.08.003
[25] Akbarov S. D, Guz' A. N. Statics of laminated and fibrous composites with curved structures. Appl Mech Rev 1992 February;45(2):17–34. https://doi.org/10.1115/1.3119747
[26] Lee J. K, Leissa A. W, Wang A. J. Vibrations of blades with variable thickness and curvature by shell theory. J Eng Gas Turb Power 1984 January;106(1):11–16. https://doi.org/10.1115/1.3239522
[27] Rafiefar M, Moeenfard H. Vibration modeling of variable thickness cylindrical shallow shells using extended Kantorovich method. Structures 2024 December;70:107554. https://doi.org/10.1016/j.istruc.2024.107554
[28] Ghannad M, Rahimi G. H, Nejad M. Z. Elastic analysis of pressurized thick cylindrical shells with variable thickness made of functionally graded materials. Compos Part B Eng 2013 February;45(1):388–96. https://doi.org/10.1016/j.compositesb.2012.09.043
[29] Hii A. K. W, Minera S, Groh R. M. J, Pirrera A, Kawashita L. F. Three-dimensional stress analyses of complex laminated shells with a variable-kinematics continuum shell element. Compos Struct 2019;229:111405. https://doi.org/10.1016/j.compstruct.2019.111405
[30] Simo J. C, Rifai M. S, Fox D. D. On a stress resultant geometrically exact shell model. part iv: variable thickness shells with through-the-thickness stretching. Comput Methods Appl Mech Eng 1990 July;81(1):91–126. https://doi.org/10.1016/0045-7825(90)90143-A
[31] Afonso S. M. B, Hinton E. Free vibration analysis and shape optimization of variable thickness plates and shells—I. finite element studies. Comput Syst Eng 1995 February;6(1):27–45. https://doi.org/10.1016/0956-0521(95)00011-N
[32] Zheng D, Du J, Liu Y. Vibration characteristics analysis of an elastically restrained cylindrical shell with arbitrary thickness variation. Thin-Walled Struct 2021 August;165:107930. https://doi.org/10.1016/j.tws.2021.107930
[33] Duan W. H, Koh C. G. Axisymmetric transverse vibrations of circular cylindrical shells with variable thickness. J Sound Vib 2008 November;317(3–5):1035–41. https://doi.org/10.1016/j.jsv.2008.03.069
[34] Carrera E, Pagani A, Zangallo F. Comparison of various 1D, 2D and 3D FE models for the analysis of thin-walled box with transverse ribs subjected to load factors. Finite Elem Anal Des 2015 March;95:1–11. https://doi.org/10.1016/j.finel.2014.10.004
[35] Carrera E, Cinefra M, Zappino E, Petrolo M. Finite element analysis of structures through unified formulation. Chichester, West Sussex, UK: Wiley; 2014 Jul.
[36] Cinefra M, Carrera E. Shell finite elements with different through-the-thickness kinematics for the linear analysis of cylindrical multilayered structures. Int J Numer Methods Eng 2012 June;93(2):160–82. https://doi.org/10.1002/nme.4377
[37] Carrera E, Pagani A, Petrolo M. Classical, refined, and component-wise analysis of reinforced-shell wing structures. AIAA J 2013 May;51(5):1255–68. https://doi.org/10.2514/1.J052331
[38] Wu B, Pagani A, Chen W. Q, Carrera E. Geometrically nonlinear refined shell theories by carrera unified formulation. Mech Adv Mater Struct 2019 December;28(16):1721–41. https://doi.org/10.1080/15376494.2019.1702237
[39] Carrera E, Pagani A, Scano D. Legendre-based node-dependent kinematics shell models for the global–local analysis of homogeneous and layered structures. Int J Solids Struct 2024;289:112630. https://doi.org/10.1016/j.ijsolstr.2023.112630
[40] Carrera E, Zappino E. One-dimensional finite element formulation with node-dependent kinematics. Comput Struct 2017;192:114–25. https://doi.org/10.1016/j.compstruc.2017.07.008
[41] Bathe KJ. Finite element procedures. Prentice Hall; 1996.
[42] Marsden J. E, Hughes T. J. R. Mathematical foundations of elasticity. Dover Publications; 1994. [Originally published in 1983 by Prentice-Hall, Englewood Cliffs, NJ].
[43] Crisfield M. A. Non-linear finite element analysis of Solids and structures. Wiley; 1996.
[44] Sahraee S, Wriggers P. Tensor calculus and differential geometry for engineers. Gewerbestrasse 11, 6330 Cham, Switzerland: Springer; 2023.
[45] Washizu K. Variational Methods in elasticity and plasticity. Headington Hill Hall, Oxford, 0X3, England: Pergamon Press; 1974.
[46] Valvano S, Carrera E. Multilayered plate elements with node-dependent kinematics for the analysis of composite and sandwich structures. Facta Univ Ser Mech Eng 2017 April;15(1):1. https://doi.org/10.22190/FUME170315001V
[47] Cinefra M, De Miguel A. G, Filippi M, Houriet C, Pagani A, Carrera E. Homogenization and free-vibration analysis of elastic metamaterial plates by carrera unified formulation finite elements. Mech Adv Mater Struct 2019 February;28(5):476–85. https://doi.org/10.1080/15376494.2019.1578005
[48] Sanchez-Majano A. R, Pagani A, Petrolo M, Zhang C. Buckling sensitivity of tow-steered plates subjected to multiscale defects by high-order finite elements and polynomial chaos expansion. Materials 2021 May;14(11):2706. https://doi.org/10.3390/ma14112706
[49] Cinefra M, Petrolo M, Li G, Carrera E. Hygrothermal analysis of multilayered composite plates by variable kinematic finite elements. J Therm Stresses 2017 August;40(12):1502–22. https://doi.org/10.1080/01495739.2017.1360164
[50] Cinefra M. Non-conventional 1D and 2D finite elements based on CUF for the analysis of non-orthogonal geometries. Eur J Mech A Solids 2021 July;88:104273. https://doi.org/10.1016/j.euromechsol.2021.104273
[51] Moruzzi M. C, Cinefra M, Bagassi S. Free vibration of variable-thickness plates via adaptive finite elements. J Sound Vib 2024 May;577:118336. https://doi.org/10.1016/j.jsv.2024.118336
[52] Li G, Carrera E, Cinefra M, de Miguel A. G, Pagani A, Zappino E. An adaptable refinement approach for shell finite element models based on node-dependent kinematics. Compos Struct 2019 February;210:1–19. https://doi.org/10.1016/j.compstruct.2018.10.111
[53] Filippi M, Carrera E, Giusa D, Zappino E. Node-dependent kinematics and multidimensional finite elements for the analysis of single/double swept, composite helicopter blades. J Am Helicopter Soc 2021 July;66(3):1–10. https://doi.org/10.4050/JAHS.66.032005
[54] Zappino E, Scano D, Carrera E. Finite element models with node-dependent kinematics based on Legendre polynomials for the global–local analysis of compact and thin walled beams. Comput Methods Appl Mech Eng 2023 October;415:116212. https://doi.org/10.1016/j.cma.2023.116212
[55] Carrera E, Zappino E, Li G. Finite element models with node-dependent kinematics for the analysis of composite beam structures. Compos Part B Eng 2018 January;132:35–48. https://doi.org/10.1016/j.compositesb.2017.08.008
[56] Zappino E, Li G, Pagani A, Carrera E, de Miguel A. G. Use of higher-order Legendre polynomials for multilayered plate elements with node-dependent kinematics. Compos Struct 2018 October;202:222–32. https://doi.org/10.1016/j.compstruct.2018.01.068
[57] Cinefra M. Formulation of 3D finite elements using curvilinear coordinates. Mech Adv Mater Struct 2020 July;29(6):879–88. https://doi.org/10.1080/15376494.2020.1799122
[58] Carrera E. C_z^0 requirements—models for the two dimensional analysis of multilayered structures. Compos Struct 1997;37. https://doi.org/10.1016/S0263-8223(98)80005-6
[59] Zappino E, Carrera E. Multidimensional model for the stress analysis of reinforced shell structures. AIAA J 2018 apr;56(4):1647–61. https://doi.org/10.2514/1.J056384
[60] Azzara R, Carrera E, Chiaia P, Filippi M, Pagani A, Petrolo M, et al. Geometrically nonlinear static analysis of multi-component structures through variable-kinematics finite elements. Acta Mech 2024 September. https://doi.org/10.1007/s00707-024-04084-w